Article:
Latta, DE, Kemner, KM, Mishra, B et al. (1 more author) (2016) Effects of calcium and phosphate on uranium(IV) oxidation: Comparison between nanoparticulate uraninite and amorphous U IV –phosphate. Geochimica et Cosmochimica Acta, 174. pp. 122-142. ISSN 0016-7037

https://doi.org/10.1016/j.gca.2015.11.010

Effects of calcium and phosphate on uranium(IV) oxidation: Comparison between nanoparticulate uraninite and amorphous U(IV)-phosphate

Drew E. Latta[a,1], Kenneth M. Kemner[a], Bhoopesh Mishra[a,b], Maxim I. Boyanov[a,c]

[a]Biosciences Division, Argonne National Laboratory, Lemont, IL 60439 USA
[b]Department of Physics, Illinois Institute of Technology, Chicago, IL 60616 USA
[c]Bulgarian Academy of Sciences, Institute of Chemical Engineering, Sofia, 1113, Bulgaria
[1]Department of Civil and Environmental Engineering, The University of Iowa, Iowa City, IA 52242 USA (Present Address)

Corresponding Author:
Drew E. Latta, Ph.D.
Biosciences Division
Argonne National Laboratory
Building 203
Lemont, IL 60439 USA

Present Address:
The University of Iowa
Dept. of Civil and Environmental Engineering
4105 Seamans Center
Iowa City, IA 52242 USA
drew-latta@uiowa.edu
ph. +1-319-936-0034

Co-Author Contact Information

Kenneth M. Kemner, Ph.D.
Biosciences Division
Argonne National Laboratory
Building 203
Lemont, IL 60439 USA
Kemner@anl.gov

Bhoopesh Mishra, Ph.D.
Biosciences Division
Argonne National Laboratory
Building 203
Lemont, IL 60439 USA
bmishra3@iit.edu

Maxim I. Boyanov
Bulgarian Academy of Sciences
Institute of Chemical Engineering
Sofia, 1113, Bulgaria
mboyanov@anl.gov

Abstract

The mobility of uranium in subsurface environments depends strongly on its redox state, with U^{IV} phases being significantly less soluble than U^{VI} minerals. This study compares the oxidation kinetics and mechanisms of two potential products of U^{VI} reduction in natural systems, a nanoparticulate UO_2 phase and an amorphous U^{IV}-Ca-PO_4 analog to ningyoite ($CaU^{IV}(PO_4)_2 \cdot 1\text{-}2H_2O$). The valence of U was tracked by x-ray absorption near-edge spectroscopy (XANES), showing similar surface-normalized oxidation rate constants for $U^{IV}O_2$ and U^{IV}-phosphate in solutions equilibrated with atmospheric O_2 and CO_2 at pH 7.0 ($k_{obs,UO2} = 0.17 \pm 0.075$ h^{-1} vs. $k_{obs,U^{IV}PO4} = 0.30 \pm 0.25$ h^{-1}). Addition of up to 400 μM Ca and PO_4 decreased the oxidation rate constant by an order of magnitude for both UO_2 and U^{IV}-phosphate. The intermediates and products of oxidation were tracked by electron microscopy, powder x-ray diffraction (pXRD), and extended x-ray absorption fine-structure spectroscopy (EXAFS). In the absence of Ca or PO_4, the product of UO_2 oxidation is Na-uranyl oxyhydroxide (under environmentally relevant concentrations of sodium, 15 mM $NaClO_4$ and low carbonate concentration), resulting in low concentrations of dissolved U^{VI} ($<2.5 \times 10^{-7}$ M). Oxidation of U^{IV}-phosphate produced a Na-autunite phase ($Na_2(UO_2)PO_4 \cdot xH_2O$), resulting in similarly low dissolved U concentrations ($<7.3 \times 10^{-8}$ M). When Ca and PO_4 are present in the solution, the EXAFS data and the solubility of the U^{VI} phase resulting from oxidation of UO_2 and U^{IV}-phosphate are consistent with the precipitation of Na-autunite. Bicarbonate extractions and Ca K-edge x-ray absorption spectroscopy of oxidized solids indicate the formation of a Ca-U^{VI}-PO_4 layer on the UO_2 surface and suggest a passivation layer mechanism for the decreased rate of UO_2 oxidation in the presence of Ca and PO_4. Interestingly, the extractions were unable to remove all of the oxidized U from partially oxidized UO_2 solids, suggesting that oxidized U is distributed between the interior of the UO_2 nanoparticles and the labile surface layer. Accounting for the entire pool of oxidized U by XANES is the likely reason for the higher UO_2 oxidation rate constants determined here relative to prior studies. Our results suggest that the natural presence or addition of Ca and PO_4 in groundwater could

slow the rates of U^{IV} oxidation, but that the rates are still fast enough to cause complete oxidation of U^{IV} within days under fully oxygenated conditions.

1. Introduction

Uranium is a toxic and radioactive element that has been used for energy generation and military purposes for several decades, resulting in stockpiles of spent fuel, mine tailings, and enrichment process waste stored at many locations around the world. Designing appropriate storage practices and predicting the effects of accidental release requires an in-depth understanding of the coupled chemical, physical, biological, and hydrological processes that control the mobility of U in oxic and anoxic environments. Developing this understanding is currently hindered by the limited availability of mechanistic information on the transformations and speciation of U under environmentally relevant conditions (Bargar et al., 2013; Burns et al., 2012; Newsome et al., 2014; Williams et al., 2013).

The solubility, and therefore the mobility, of uranium is strongly affected by its valence state. In oxidizing environments uranium is stable as U^{VI}. When equilibrium with schoepite ($UO_3 \cdot 2H_2O$) controls U^{VI} solubility, the resulting aqueous concentrations are on the order of 10^{-4} M at pH 7 (Jang et al., 2006). In reducing environments uranium is stable as U^{IV}. When equilibrium with uraninite (UO_{2+x}) controls U^{IV} solubility, the resulting aqueous concentrations are on the order of 10^{-8} M at pH 7 (Ulrich et al., 2008). The dramatic decrease in solubility in this simplified scenario is expected to significantly influence U mobility in the subsurface and has been the impetus for extensive research on (bio-) reduction of U^{VI} for the purpose of contaminated site remediation. However, uranium transformations in the subsurface occur in the presence of various surfaces and dissolved ions, which can affect the solubility, speciation, and outcome of reactions with U. For instance, carbonate forms strong, highly soluble complexes with U^{VI} and together with Ca^{2+} decreases the ability of U^{VI} to be reduced to U^{IV} (Brooks et al., 2003). Phosphate and phosphatase activity influences U^{VI} solubility through the formation of precipitates (Beazley et al., 2007), which can affect the rate of U^{VI} bioreduction (Rui et al., 2013). U^{VI} can interact with various mineral and biological surfaces to form stable adsorption complexes (Bargar et al., 1999; Kelly et al., 2002). The complexity in U^{VI} speciation described above is accounted for in most transport models. However, only an amorphous uraninite phase is typically used to model the behavior of reduced U^{IV},

92 under the assumption that the lowest solubility mineral controls U^{IV} dynamics (Li et al., 2010; Li et al.,
93 2009; Yabusaki et al., 2007a). Research in the past few years has drawn this assumption into question, at
94 least for processes occurring over the months-to-years timescale. Low levels of phosphate were shown to
95 inhibit the formation of uraninite during U^{VI} reduction, resulting in non-uraninite, phosphate-complexed
96 U^{IV} solid phases (Alessi et al., 2014b; Boyanov et al., 2011; Stylo et al., 2013). Investigations of U
97 speciation in reduced sediments and soils also indicates the prevalence of non-uraninite U^{IV} species over
98 uraninite, although the exact identity of U^{IV} species remains unclear (Alessi et al., 2014a; Bargar et al.,
99 2013; Li et al., 2015; Wang et al., 2014). Recently, high-affinity mineral surface sites were shown to
100 stabilize mononuclear U^{IV} adsorption complexes and thus inhibit uraninite formation (Latta et al., 2014).
101 Subsequent work developed a surface complexation model and determined stability constants for such
102 sites (Wang et al. 2015). These developments indicate a significant gap in the description of short-term
103 U^{IV} dynamics in transport models and suggest the need for the study of non-uraninite U^{IV} reactions in
104 model systems so appropriate reactions can be included in the more complex field-scale models (Long et
105 al., 2015).

106 Of particular importance to U stability under the changing redox conditions in natural
107 environments is the oxidation of U^{IV} phases, as U^{VI} species have a much higher potential for
108 remobilization. Oxidation can occur due to the influx of dissolved oxidants, as well as due to water
109 radiolysis under anoxic conditions (Ekeroth and Jonsson, 2003; Ulrich et al., 2008). A number of studies
110 have addressed uraninite oxidation in batch and electrochemical experiments from the perspective of
111 nuclear fuel corrosion, providing a detailed and mechanistic understanding of the process (Roth and
112 Jonsson, 2008; Shoesmith, 2000) and references therein). Electrochemical studies coupled with surface
113 sensitive x-ray photoelectron spectroscopy have shown that UO_2 oxidation proceeds via surface oxidation
114 to $UO_{2.33}$, followed by accumulation of surface UO_2^{2+} layers as oxidation further progresses (Shoesmith,
115 2000; Shoesmith et al., 1989). Accumulation of surface U^{V}/U^{VI} hinders the interpretation of batch and
116 flow UO_2 oxidation experiments. Surface layers of $UO_{2.33}$ do not form under high-bicarbonate conditions

because U^{VI} dissolves directly to solution (Shoesmith, 2000; Ulrich et al., 2009). Hence, most electrochemical studies have used high bicarbonate concentrations to provide meaningful results for UO_2 oxidation and dissolution. On the other hand, electrochemical studies only measure electron transfer reactions, and thus require supporting evidence such as spectroscopic or diffraction data to provide comprehensive information about non-redox phase transformations.

More recent studies have looked at the oxidation of uraninite from the perspective of U release following reductive remediation. Consistent with electrochemical studies on UO_2 spent fuel corrosion, several studies of UO_2 dissolution after reductive immobilization have found that carbonate increases the rate of oxidative UO_2 dissolution through promotion of U^V/U^{VI} surface layer detachment (Pierce et al., 2005; Ulrich et al., 2009). Interestingly, Ulrich and coworkers found that biogenic nanoparticulate uraninite dissolved at a similar surface-area-normalized rate as larger particles of synthetic UO_2, but nanoparticulate UO_2 supported a higher concentration of U in solution during oxidation, presumably due to higher surface strain in the smaller particles. Several studies to date have shown that mass transport has important effects on the mobility of U in subsurface systems, and have found that the release of U^{VI} from UO_2 is slowed in diffusion limited and advective systems relative to mixed batch reactors (Campbell et al., 2011; Giammar et al., 2012).

In contrast to the extensive studies of UO_2 oxidation, very limited information is available on the stability and oxidation of non-uraninite U^{IV} phases. U^{IV} in biogenic, non-uraninite solids was found more labile to dissolution than uraninite in 1 M anoxic bicarbonate extractions (Alessi et al., 2012). Interpretation of U^{IV} release in bicarbonate extractions, however, may be complicated by reversal of the electron transfer between U^{IV} and the oxidized reductant of U^{VI} (e.g., organic matter, electron shuttles, or Fe^{3+}) (Ginder-Vogel et al., 2006; Stoliker et al., 2013), leading to U^{IV} oxidation and release of U^{VI}. Cerrato et al. (2013) studied the oxidation of a biogenic, non-uraninite phase at lower bicarbonate concentrations (100 mM) and concluded comparable oxidation rates for biogenic uraninite and non-uraninite U^{IV} species. A slight preference for oxidation of non-uraninite U^{IV} species relative to uraninite

142 was suggested in experiments with mixtures of these two phases. Sharp et al. (2011) investigated the
143 oxidative release of U from non-uraninite U^{IV} species in sediments that have been previously subjected to
144 reducing conditions and U^{VI}-containing influents. The authors concluded that these U^{IV} species were less
145 stable than biogenic uraninite under both anoxic and oxic conditions. Despite these initial results, the
146 knowledge about the stability of non-uraninite U^{IV} phases appears to be far from a state where specific
147 reactions can be included in reactive transport models.

148 Here, we investigate the rates and products of the oxidation of a non-uraninite, amorphous U^{IV}-
149 phosphate phase by dissolved oxygen (DO), under environmentally relevant conditions. The results are
150 compared to the oxidation of nanoparticulate uraninite under the same conditions. The goal was to obtain
151 insight on the oxidation mechanisms and to estimate the relative stability of the two U^{IV} phases in
152 controlled experiments. We examined the effect of Ca^{2+} and HPO_4^{2-} on U^{IV} oxidation; both are ions that
153 are ubiquitous and are typically in excess of U in natural environments, thus potentially affecting uranium
154 geochemistry. Elevated Ca^{2+} and PO_4 concentrations also create conditions that inhibit U^{VI} dissolution,
155 allowing for control of the surface dissolution step in the overall oxidation process and providing
156 information on the mechanism of oxidation. Unlike previous studies, which determined the rate of U^{IV}
157 oxidation from the rate of oxidant consumption or from the rate of U^{VI} dissolution, here we determined
158 the change in U^{IV}/U^{VI} content over time from x-ray absorption spectroscopy measurements. This
159 approach provides a direct measurement of U^{IV} oxidation in the hydrated solids under the conditions of
160 interest, as well as information on the reaction products and intermediates. In such a way, the U^{IV}
161 oxidation reaction was studied without potential interfering factors such as rate-limiting dissolution of the
162 oxidized products or solution conditions that may favor oxidized U dissolution but alter U speciation and
163 reaction dynamics. In addition, potential artifacts from drying of the samples or from unaccounted oxidant
164 consumption in parallel reactions not related to U^{IV} oxidation are eliminated.
165
166

2. Methods and materials

2.1. Synthesis of U^{IV} solids

Uranium^{IV} solids were synthesized by chemical reduction of uranyl-carbonate solutions using 9,10-anthrahydroquinone-2,6-disulfonic acid (AH_2QDS). A 25 mM stock solution of AH_2QDS was prepared by reduction of 25 mM 9,10-anthraquinone-2,6-disulfonic acid (AQDS) by H_2 in the presence of a Pd catalyst (0.5 wt% on Al_2O_3 supports). AH_2QDS stock solutions were filtered prior to use. Uranyl chloride was used as the starting U^{VI} stock, and was synthesized by dissolving UO_3 in HCl to prepare a stock with an approximate uranium concentration of 0.1 M UO_2^{2+}. All U^{IV} solids were synthesized inside an anoxic chamber with a 3% H_2/97% N_2 atmosphere with a Pd oxygen scrubbing catalyst (<1ppm O_2 at all times). Deionized water used in the anoxic chamber was deoxygenated by bubbling with N_2 for 2 hours, and left open overnight in the chamber to complete the removal of trace O_2.

2.1.1. Uraninite synthesis

Uraninite was synthesized from a uranyl-carbonate solution using AH_2QDS as a reductant for U^{VI}. A solution of 0.5 mM U^{VI} was prepared by adding 0.5 mL of 0.1 M uranyl chloride stock to 100 mL of 5 mM $NaHCO_3$ solution. After addition of the uranyl solution, the pH was adjusted to a value of 7.1 with 1 M NaOH. To initiate the reduction of U^{VI}, 9.6 mL of the 25 mM AH_2QDS stock was added to the uranyl-bicarbonate solution. The reactor was shaken to mix the reactants, then capped, and the pH was adjusted with 1 M NaOH or HCl and allowed to react for 24 hours. After a day of reaction time, the uranium solids were harvested by filtration (0.22 μm membrane filter). The filtered solids were resuspended in ~10 mL of deionized water in a serum vial and dispersed from the filter membrane using a bath-style sonicator. The total uranium content after digestion and oxidation of the suspension was measured by kinetic phosphorescence analysis (KPA-11, Chemchek Instruments, Inc.) using URAPLEX as the complexant. Kinetic phosphorescence analysis is specific to U^{VI}, and samples were prepared by dissolving 50 μL of the U^{IV} suspension in 200 μL 5 M H_2SO_4 for 1 hour, diluting to a total volume of 1

mL by addition of deionized (DI) water, and oxidizing the U^{IV} overnight (≈18 hours) in micro-centrifuge tubes removed from the anoxic glove box and exposed to air. Triplicate analyses indicated that the total U concentration in the uraninite suspension was 4.43 ± 0.113 mM (1 σ).

2.1.2. U^{IV}-phosphate synthesis

A ningyoite-like (ningyoite: $CaU(PO_4)_2 \cdot H_2O$) U^{IV}-phosphate solid was synthesized from a uranyl-carbonate solution containing Ca^{2+} and PO_4^{3-} using AH_2QDS as a reductant. Here, a solution of 30 mM $NaHCO_3$ was prepared by adding 13.5 mL of 1 M $NaHCO_3$ to 410 mL DI water. U^{VI} was added using 0.45 mL of the 0.1 M uranyl chloride stock for a final concentration of 100 μM. Then 1.35 mL of 0.1 M NaH_2PO_4 was added to the solution for a final concentration of 300 μM PO_4^{3-}. A 1.05-mL aliquot of 0.043 M $CaCl_2$ was added last to minimize the possibility for Ca-PO_4 precipitation. The final Ca^{2+} concentration was 100 μM. The pH of the U^{VI}-Ca^{2+}-PO_4^{3-}-CO_3^{2-} solution was adjusted to 6.9, and 24 mL of 25 mM AH_2QDS stock was added to initiate the reduction reaction (final [AH_2QDS] = 1.33 mM). The pH was checked after AH_2QDS addition, and readjusted to a value of 6.9 with 1 M NaOH and 1 M HCl. After 1 day of reaction time, the U^{IV}-phosphate solids were collected by filtration and the solids on the membrane were dispersed into DI water by sonication. As with uraninite, total U in the suspension was measured with the KPA after dissolution of 50 μL of the suspension in 200 μL 5 M H_2SO_4, subsequent dilution to 1 mL, and oxidation of U^{IV} to U^{VI} in air. Analysis of triplicate samples indicated that the concentration of total U in the suspension was 3.12 ± 0.241 mM (1 σ). Mean calcium concentration in the solids suspension (from two samples) measured by inductive coupled plasma-optical emission spectroscopy (ICP-OES) was 1.32 mM.

2.1.3. U^{VI} solids synthesis

Two U^{VI} samples were prepared to provide reference spectra of the possible oxidation endmember phases for the x-ray absorption spectroscopy (XAS) analysis. A U^{VI} oxyhydroxide sample

was prepared by adding 0.1 M U^{VI}-chloride stock to the 3-(N-morpholino)propanesulfonic acid (MOPS)/$NaClO_4$ buffer for a nominal U^{VI} concentration of 0.5 mM, and adjusting the pH of the solution to approximately 7.0 with 0.5 M NaOH. A colloidal precipitate formed at this pH value and after 24 hours of reaction under stationary conditions the solution was filtered and the solids mounted as described above. A U^{VI} phosphate sample was prepared under solution conditions similar to those of the oxidation experiments: 100 μM U^{VI}, 400 μM Ca^{2+}, and 400 μM PO_4^{3-} at pH 7.2. Here, U^{VI} stock was added to the MOPS/$NaClO_4$ buffer containing 400 μM Ca and PO_4^{3-}. The precipitate was filtered after 3 days of reaction and mounted for XAS analysis as with other samples.

2.2. Experimental procedures

2.2.1. U^{IV} oxidation experiments

Prior to the oxidation experiments, the phase identity of each batch of the starting U^{IV} materials was verified using EXAFS (Fig. EA-7). Oxidation of the two U^{IV} solids—uraninite and the ningyoite-like U^{IV}-phosphate—was performed in 5 mM MOPS buffer with 15 mM $NaClO_4$ as the background electrolyte and 100 μM of U^{IV} solids. The pH of the solution was set at pH 7.0 by using appropriate quantities of MOPS-acid and its sodium salt. The experiment consisted of a series of sacrificial batch reactors with each reactor representing a separate time point and treatment. Each reactor was prepared in a 60-mL glass serum bottle open to ambient atmosphere filled with 25 mL of the buffer/electrolyte solution. Initial dissolved oxygen in the buffer at 22°C was measured to be 237 μM O_2 using an Orion 3-Star Portable DO meter (Thermo Scientific).

Experiments with uraninite included uraninite oxidation without calcium and phosphate, and experiments that included 400 μM Ca^{2+} and/or 400 μM PO_4^{3-}. U^{IV}-phosphate oxidation experiments were done without added Ca or PO_4^{3-}, as well as with 100 μM and 400 μM added Ca^{2+} and PO_4^{3-}. Addition of the U^{IV}-PO_4 solid to the buffer added 42 μM Ca and 105 μM PO_4. Immediately prior to initiation of the experiments, Ca and PO_4^{3-} were added from a 100 mM $CaCl_2$ stock and a 100 mM PO_4^{3-} stock prepared

241 from 0.062 M NaH_2PO_4 and 0.038 M Na_2HPO_4 to have a pH value near 7.0. Bottles were crimped with a
242 butyl-rubber stopper to seal in an ambient atmosphere headspace, and transferred into the anoxic
243 chamber.

244 Oxidation of U^{IV} was initiated by spiking the sealed oxygen-containing serum-vials with U^{IV}
245 suspensions in the glove box. Aliquots of uraninite and U^{IV}-phosphate suspensions were measured out
246 with a pipette into a micro-centrifuge tube, loaded into needle-tipped syringes, and injected into the serum
247 vials to initiate the oxidation reaction. Reactors were shaken by hand to suspend the solids in the buffer,
248 and transferred within 2 minutes to a shaker table operating at 175 rpm outside of the anoxic chamber.
249 Nominal reaction times between 10 minutes and 72 hours were chosen to trace the kinetics of U^{IV}
250 oxidation. Reaction time was recorded with a precision of 1 minute. Samples reacted for 10 and
251 30 minutes were not transferred out of the anoxic chamber, but were shaken vigorously by hand every 2–
252 3 minutes to maintain oxygen equilibrium between the gas and liquid phase. The initial concentration of
253 O_2 in the air-equilibrated solutions is 0.237 mM, which is sufficient to oxidize 0.948 mM of U^{IV}. The total
254 reservoir of O_2 in the aqueous and gas phase was 1.45 mmoles, which is 290 times greater than the 5
255 µmoles of O_2 required to completely oxidize the amount of U^{IV} present. The oxidation reaction can
256 therefore be assumed to be pseudo-first order with respect to the oxidant. Un-oxidized U^{IV} solids controls
257 were prepared in a similar fashion, but in an anoxic buffer solution prepared by bubbling with Ar for 2
258 hours. Control vials were not removed from the anoxic chamber over the course of the experiments.

259 Prior to sampling, reactors were transferred back into the anoxic chamber and approximately
260 15 mL of suspension was filtered through a 0.22 µm membrane filter. The filtered solution was saved for
261 Ca, PO_4^{3-}, and U analysis. The filtered solids were sealed together with the filter membrane between two
262 layers of Kapton film for x-ray absorption spectroscopy analysis.
263

264 **2.2.2. Bicarbonate extractions**

A series of extraction experiments (100 mM $NaHCO_3$, pH 8.2) were conducted to probe whether a passivation layer of U^{VI} formed on the surface of UO_2 during oxidation in the presence of 400 μM Ca and PO_4. These experiments also tested whether removal of this oxidation layer affected subsequent U^{IV} oxidation. To start, a suspension of UO_2 was prepared and oxidized as described above: a 250-mL bottle filled with 150 mL of solution containing 5 mM MOPS, 15 mM $NaClO_4$, and 400 μM Ca, and PO_4 was equilibrated with 100 mL ambient atmosphere headspace. The sealed bottle was spiked with 100 μM U^{IV} as UO_2 and placed for 10 hours on an orbital shaker, then transferred back to the anoxic glove box and sub-sampled for analysis of U valence state prior to extraction. The remaining solids were collected by filtration through a 0.22 μm nylon membrane, suspended in 60 mL of anoxic 100 mM $NaHCO_3$ adjusted with HCl to pH 8.20, and sonicated to disperse the particles. The bottle was crimp-sealed and placed on an orbital shaker for 14.5 hours.

After extraction, an aliquot was filtered and mounted for XAS analysis of U valence state. The remaining solids were again collected by filtration, washed by passing approximately 20 mL of deoxygenated DI water over the filtered solids, and re-suspended in 4 mL deoxygenated DI water by sonication. Appropriate aliquots of the suspension were dispensed to reactors containing oxic 25-mL MOPS/$NaClO_4$ solutions for oxidation experiments identical to the ones described above with unextracted UO_2. Results were compared between reactors with and without added Ca and PO_4 in the solution phase.

2.3. Solids characterization

2.3.1. Electron microscopy

The U solids in some of the samples were imaged with scanning electron microscopy (SEM). Solids were centrifuged from 2-mL aliquots of the reactors and suspended in 0.1 mL of deoxygenated methanol. The suspensions were then spread onto 12.7-mm graphite stubs (Ted Pella, Inc.) and dried for 12 hours in the anoxic chamber in a sealed desiccator using calcium sulfate as a desiccant (Drierite). The

289 dried samples were only briefly exposed to oxygen when transferring them from an anoxic transport box
290 to the SEM. Samples were imaged using a Quanta 400F Environmental SEM (FEI Company) operating
291 under high-vacuum conditions and an accelerating voltage of 3 to 5 kV. Secondary electron images were
292 collected using an Everhart-Thornley detector. Energy dispersive x-ray spectroscopy (EDS) fluorescence
293 spectra were produced using an electron accelerating voltage of 20 kV and collected using a Revolution
294 EDX spectrometer and software (4pi Analysis, Inc.). The x-ray fluorescence spectra were collected for 60
295 s while rastering the electron beam on the sample, resulting in spectra averaged over the imaged area.
296 Transmission electron microscopy (TEM) was used to determine the morphology and particle
297 sizes of the uraninite and U^{IV}-phosphate starting materials, which were then used as a basis to calculate
298 specific surface area. Samples were prepared as described above for SEM analysis, and dropped onto
299 ultra-thin holey carbon copper supported TEM grids. Samples were imaged with a FEI CM30T
300 microscope using an accelerating voltage of 200 kV and a Gatan charge-coupled device camera. For
301 nearly spherical nanomaterials, TEM surface area is statistically similar to BET surface area (Bau et al.,
302 2010).
303
304 **2.3.2. X-ray absorption spectroscopy (XAS)**
305 The hydrated solids from both unoxidized and oxidized reactors were analyzed by x-ray
306 absorption spectroscopy to probe the oxidation state and the coordination environment of U and Ca using
307 the x-ray absorption near-edge structure (XANES) and the extended x-ray absorption fine structure
308 (EXAFS) regions of the spectrum, respectively. Measurements at the uranium L_{III} edge (17,166 eV) were
309 done at the MRCAT/EnviroCAT bending magnet and insertion device beamlines (sector 10-BM and 10-
310 ID) at the Advanced Photon Source, Argonne National Laboratory. The experimental setup at these two
311 beam lines is reviewed in prior work (Kropf et al., 2010; Segre et al., 2000). As described above, the
312 filtered and hydrated solids were sealed between Kapton film and were maintained under anoxic
313 conditions until measurement. Spectra were recorded at room temperature in transmission and

fluorescence modes using gas-filled ionization chambers. Samples were maintained in a N_2-flushed chamber during measurement to preclude oxidation by ambient O_2. Data consistency was confirmed by scanning three fresh locations on each sample, with at least two scans taken at each location. No evolution of oxidation state was observed in successive scans, indicating that beam-induced redox changes were negligible or absent. Spectra were averaged to produce the final data.

The raw spectra were normalized and background was subtracted using the program Athena (Ravel and Newville, 2005). Linear combination fits of the XANES and EXAFS spectra were carried out to quantify the proportions of U^{IV} and U^{VI} endmembers in the samples at different time points during oxidation. The statistical uncertainty from the numerical fits was reported by Athena as less than 2% for all fits; however, this estimate does not account for possible differences between the phases present in the sample and those used as endmembers in the fit. Due to the high quality of the data and the known endmembers we estimate an overall uncertainty of ±5% in the data reported in Fig. 1 and Table 2.

Calcium K-edge XAS spectra were collected at room temperature at the MRCAT/EnviroCAT bending magnet beamline in fluorescence mode using a four-element silicon drift detector. To maximize Ca fluorescence intensity, the sample and detector were placed in close proximity within a He purged chamber. Samples were mounted and sealed using Scotch (3M Corporation) brand tape, as preliminary measurements indicated that Kapton tape typically used to mount XAS samples contained a Ca contaminant. The energy was calibrated at 4038.5 eV to the inflection point of a spectrum from calcite ($CaCO_3$). Standards included a 1 M solution of $CaCl_2$ (as a standard of O-coordinated Ca^{2+}) and calcium phosphate (hydroxyapatite). The latter was synthesized by mixing equal parts of 10 mM $CaCl_2$ and NaH_2PO_4 solutions and titrating the solution to pH 7.1. The turbid solution was allowed to age overnight, centrifuged and washed twice with DI water, then stored as a suspension in DI water for a month prior to use.

2.3.3 XRD measurements

339 Powder x-ray diffraction (pXRD) patterns were measured from selected UO_2 and U^{IV}-phosphate
340 solids after oxidation. Data were collected using a Rigaku MiniFlex diffractometer using Cu K-alpha
341 radiation with a Ni K-beta filter. Long scans (8 s per 0.02 °2θ) were used because of the small amount of
342 solids available. Samples were mounted on aluminum sample holders in the glove box and covered with a
343 drop of glycerol and a thin layer of polyethylene film to prevent oxidation; pXRD was also used to
344 confirm the identity of the calcium phosphate standard (hydroxyapatite).
345
346 **2.4. Solution analysis**
347 **2.4.1. KPA analysis of total uranium**
348 Solution samples from the uranium oxidation experiments were analyzed using kinetic
349 phosphorescence analysis with a KPA-11 analyzer (Chemchek Instruments, Inc.). Total dissolved
350 uranium was measured using a wet-ashing technique to remove interfering solution constituents (MOPS
351 buffer and Cl^-). Glass sample vials (1 mL) were cleaned using a 1:1 dilution of trace-metals grade
352 concentrated HNO_3 in water at 40°C for 12 hours, then washed with deionized water and dried. Each vial
353 was filled with 500 µL of sample solution, 100 µL 30% H_2O_2, and 400 µL trace-metals grade
354 concentrated HNO_3, and was evaporated to dryness in a heating block set to 90°C inside a fume hood.
355 After wet-ashing, the samples were reconstituted to 1 mL with 1 M nitric acid (trace metals grade). A
356 250-µL aliquot of each sample was placed in a quartz cuvette and diluted to 1 mL with DI water, to which
357 1.5 mL of URAPLEX (Chemchek Instruments, Inc.) reagent was added. A 1 M nitric acid blank (1 mL)
358 contained 4.25 ppb U, and uranium detections below this level were consistent with dilution of this
359 quantity of U by 250 µL of sample. These are reported as less than the blank in Table 2.
360
361 **2.4.2. ICP-OES analysis of total uranium, calcium, and phosphorus**
362 Samples from oxidation experiments were analyzed concurrently for total uranium, calcium, and
363 phosphorus (phosphate) using inductively coupled plasma-optical emission spectroscopy (Perkin-Elmer

4300DV ICP-OES). Samples were diluted into 10 mL of 5% HNO_3, to which 3 mL of a 1 ppm Y in 5% HNO_3 was added as an internal standard. Uranium was quantified using the emission line at 385.958 nm, calcium at 317.933 nm, and phosphorus at 213.617 nm.

3. Results and Discussion

3.1. Oxidation of U^{IV} solids by dissolved O_2

3.1.1 Oxidation of U^{IV} in nanoparticulate uraninite and in U^{IV}-phosphate

Here we present the results from the oxidation of nanoparticulate uraninite and amorphous U^{IV}-phosphate in closed systems with dissolved oxygen (O_2) and carbonate concentrations resulting from equilibrium of the initial solution with air (approximately 250 μM O_2 and 100 μM HCO_3; air in the headspace). Suspensions with 100 μM U^{IV} were oxidized at pH 7.0 buffered by 5 mM MOPS in 15 mM $NaClO_4$ background electrolyte. U in the solution phase of all systems was less than 0.3% of total U at all stages of the 72 h oxidation process (dissolved U < 0.22 μM, Table 2). The changes in oxidation state of solid phase U were tracked by XANES. In all systems, the trend in the spectra with reaction time is a progressive shift of the absorption edge to higher binding energies, indicating an increase in the average valence state of U (Fig. EA1-EA5). The XANES overlays for the U^{IV}-phosphate system (Fig. EA3) exhibit isosbestic points, suggesting transformation between one U^{IV} and one U^{VI} endmember, without detectable (i.e., >5% of total U) intermediate phases. In contrast, experiments with uraninite do not show consistent isobestic points (Fig. EA1), suggesting that oxidation of uraninite may go through an intermediate phase prior to formation of the U^{VI} endmember. We discuss this result later in a discussion of the oxidized U products.

The kinetics of U^{IV} oxidation, shown as U^{IV}/U_{total} in the solids over time, are summarized in Fig. 1 and Table 1. The U^{IV}/U_{total} ratios were determined by linear combination fits of the XANES spectra using

389 the starting U^{IV} materials and the observed final U^{VI} phases as endmembers (U^{VI}-oxyhydroxide for
390 uraninite and autunite for U^{IV}-phosphate, respectively). We assume that the kinetics of U^{IV} oxidation are
391 pseudo-first order with respect to oxygen concentration (total oxygen in the system was 290 times the
392 amount required for complete oxidation to U^{VI}, i.e., $\Delta O_2 < 0.3\%$). Using log-linear regression
393 ($ln(U^{IV}/U_{total})$ vs. time), we estimate the average rate constants for the initial oxidation (i.e. the first 4
394 points) of uraninite and U^{IV}-phosphate to be $k_{obs,UO2} = 0.17 \pm 0.075$ h^{-1} (standard deviation of triplicate
395 experiments) and $k_{obs,U^{IV}PO4} = 0.30 \pm 0.25$ h^{-1} (duplicate experiments), which indicates that oxidation rate
396 constants are similar for the two materials (Fig. 1 and Table 1). In experiments with different batches of
397 U^{IV} solids, we found that the oxidation rate constants of both UO_2 and U^{IV}-phosphate vary over a factor of
398 2 to 4, most likely due to batch-to-batch variability in the morphology of the synthesized U^{IV} materials
399 (the atomic structure as determined by EXAFS was the same between batches, Fig. EA-7).
400 We attribute some of the difference in apparent oxidation rate constants between UO_2 and U^{IV}-
401 phosphate to differences in particle size between the two solids. The particle sizes of uraninite and U^{IV}-
402 phosphate determined by TEM show that uraninite formed primary particles on average 3.5 nm in
403 diameter, whereas U^{IV}-phosphate formed primary particles approximately 12–16 nm in diameter (Fig.
404 EA6). Calculated surface areas (assuming a spherical particle) are 160 m^2 g^{-1} and 40 to 100 m^2 g^{-1}
405 depending on the batch, respectively for UO_2 and U^{IV}-phosphate. Particle sizes on the second and third
406 batches of uraninite were not measured. Given the uncertainties generally associated with rate constant
407 and surface area determinations (e.g., batch-to-batch variability of the starting materials or differences in
408 aggregation state modulating the reactive surface area), the difference of up to 4 times in rate constants
409 suggests that, under the tested conditions, the oxidation rates of UO_2 and U^{IV}-phosphate are not greatly
410 different and could be related to differences in particle sizes.
411 In order to compare our U^{IV} oxidation rates to previous work we estimated the initial oxidation
412 rate of U^{IV} in our study from the slope of initial change of U^{IV}/U_{total} vs. time (Cerrato et al., 2013). Our
413 average oxidation rates of 2.2×10^{-7} mol (g U)$^{-1}$ s^{-1} for U^{IV}-phosphate and 7.3×10^{-7} mol (g U)$^{-1}$ s^{-1} for

UO_2, are slower by a factor of approximately 4.5 relative to those determined in Cerrato et al., where biomass-associated U^{IV}-phosphate oxidized slightly faster (9.9×10^{-7} mol (g U)$^{-1}$ s^{-1}), but were similar for biogenic UO_2 (6.2×10^{-7} mol (g U)$^{-1}$ s^{-1}) (Cerrato et al., 2013). Our results are also consistent with those reported by Sharp and coworkers for oxidative release of U from sediment microcosms containing U^{IV} bound to phosphate or carbonate (Sharp et al., 2011). In that study, U^{IV} oxidation and release was modeled using two pools of U^{IV} with oxidative release rates of 5.5×10^{-5} mol (g U)$^{-1}$ s^{-1} and 8.1×10^{-7} mol (g U)$^{-1}$ s^{-1} (Sharp et al., 2011). In spite of different measurement methods of U^{IV} oxidation—U dissolution in the previous studies and solid U valence state by XANES here—the data from our study and those of Cerrato et al. and Sharp et al. are consistent. Overall, the additional data from our study confirms that under relatively simple solution conditions, U^{IV} oxidation in bulk precipitates of U^{IV}-phosphate and nanoparticulate UO_2 proceeds at rates that are within an order of magnitude of each other.

We also estimated initial surface-area normalized rate constants ($k_{SA} = k_{obs}$/surface area loading) in order to compare to those tabulated for large particulate UO_2 in Roth and Jonsson (2008). Here surface area normalized rate constants for UO_2 oxidation (1 to 2.7×10^{-8} m s^{-1}) are 1 to 2 orders of magnitude higher than those tabulated for O_2-mediated oxidation of large UO_2 particles (3×10^{-9} to 3.6×10^{-10} m s^{-1}) (Roth and Jonsson, 2008). Although Cerrato et al. (2013) did not report specific surface area for the nanoparticulate solids used in their study, we calculated surface-normalized rate constants from the oxidation data (by using our TEM surface area for their similarly sized biogenic UO_2 particles of about 3.5 nm diameter). The data from Cerrato et al. suggests surface area normalized rates that are up to an order of magnitude greater for biogenic UO_2 with a particle of size of 3.5 nm (~2 to 5×10^{-9} m s^{-1}) than for chemogenic UO_2 (1×10^{-10} m s^{-1}) with a particle size of 100–200 nm. The differences in UO_2 surface-area normalized rates between our study, Cerrato et al.'s study, and the studies reviewed in Roth and Johnson (2008) may be due to a surface strain effect on reactivity resulting from the small particle size, as well as uncertainty in surface area estimation. Nanoparticulate UO_2 is likely more susceptible to oxidation, given that it also dissolves significantly faster than micron-sized UO_2 particles (Cerrato et al.,

2013; Roth and Jonsson, 2008; Ulrich et al., 2009). In addition, previous studies used (bi)carbonate extractions to solubilize oxidized U and assumed that U release was limited by U^{IV} oxidation (Cerrato et al., 2013; Roth and Jonsson, 2008). While the assumption of prompt dissolution of U^{VI} from the surface is likely a valid one, it is possible that U^{V}/U^{VI} present within the particles is released more slowly; this pool of oxidized U in the system is not captured by the bicarbonate extractions, but is observable in the x-ray spectroscopy measurements used here (discussed below).

3.1.2. Solution dynamics during oxidation

In addition to tracking U valence in the solids, we also measured dissolved U, Ca, and P (Table 2). We observed insignificant release of U to solution in all systems; dissolved U concentrations were below 2.5×10^{-7} M at all times (<0.3% of total U). The variability observed at these low concentrations is likely a separation artifact resulting from small amounts of solids passing through the filter and subsequently dissolving during the acidification of the aqueous samples. The range of measured U concentrations for each system is compared to equilibrium solubility calculations for several oxidized U phases in Fig. 2, with the understanding that the precipitated U^{VI} minerals may be in a metastable state.

Interestingly, the measured U concentrations for the UO_2 oxidation experiments are 3 orders of magnitude lower than those expected for U^{VI} in equilibrium with schoepite (calculation shown in Fig. 2A for our experimental conditions: 15 mM $NaClO_4$, pH 7.0, ~100 μM dissolved bicarbonate from equilibrium with ~400 ppm CO_2 in the headspace air). Other U^{VI} precipitates considered for our 15 mM Na^+ systems were a low-temperature clarkeite-like solid studied by Giammar and Hering ($K_{sp} = [UO_2^{2+}][Na^+]/[H^+]^3 = 10^{8.81}$) and a Na-compreignacite phase studied by Gorman-Lewis et al. ($K_{sp} = [Na^+]^2[UO_2^{2+}]^6/[H^+]^{14} = 10^{39.4}$) (Giammar and Hering, 2004; Gorman-Lewis et al., 2008). The measured U^{VI} concentrations in our work are closer to those resulting from with the clarkeite-like solid than with schoepite or Na-compreignacite. The low solubility of sodium-containing uranyl phases may be of importance in oxic groundwater containing significant amounts of dissolved sodium and low bicarbonate

concentrations. For example, the U.S. Department of Energy (DOE) U-contaminated sites at Rifle, Colorado, and Oak Ridge, Tennessee, have approximately 10–30 mM dissolved Na^+ (Revil et al., 2013; Zachara et al., 2013). Such Na-bearing phases may control U solubility in rock salt formations used for U-bearing waste interment such as the Waste Isolation Pilot Plant (Goldstein, 2011), and during corrosion of UO_2 reactor fuel exposed to ocean water at the Fukushima nuclear incident site (Burns et al., 2012).

Oxidation of the U^{IV}-phosphate solids results in aqueous U concentrations below 7.3×10^{-8} M at all times (Table 2). Calcium concentrations in solution are relatively constant over the course of the experiment (16 to 23 μM). The Ca remaining in the solids after 72 hours of oxidation is 46% of the Ca present in the initial solids, suggesting that some calcium is retained in the oxidized solids. In contrast to Ca, aqueous phosphate concentrations increase from 10.5 μM in the control to 17.7 μM after 9 hours of oxidation but decrease to only 2.1 μM after 72 hours, suggesting a near-complete incorporation of the available 100 μM phosphate into the products of oxidation. Retention of Ca and PO_4 in the solids is consistent with the precipitation of autunite phases (autunites are $X_{1,2}(UO_2)_2(PO_4)_2 \cdot 8–11H_2O$, where X are mono- or di-valent metals). The measured concentrations of U in solution are within the range of calculated U solubilities from Na-autunite for the conditions in this study (2–18 μM PO_4, 400 ppm CO_2, and 15 mM Na^+; Fig. 2B). Overall, the solution dynamics of U, Ca, and phosphate suggest that oxidation of U^{IV}-phosphate results in low-solubility U^{VI}-phosphate phases; this is also supported by the spectroscopic and pXRD evidence discussed below.

3.1.3. Products of UO_2 and U^{IV}-phosphate oxidation

The solubility of U^{VI} in our study suggests the formation of Na-uranyl oxyhydroxides and Na-uranyl phosphates upon oxidation of UO_2 and U^{IV}-phosphate, respectively. The speciation of U in the solids is presented below, as determined by EXAFS, scanning electron microscopy with elemental dispersive x-ray analysis (SEM-EDX), and powder x-ray diffraction (pXRD).

488 The EXAFS spectra of the solids in all systems after 72 hours of oxidation are compared to
489 spectra from U^{VI}-oxyhydroxide and U^{VI}-phosphate standards (Fig. 3). The EXAFS spectrum of UO_2
490 oxidized for 72 hours is the same as that of the U^{VI} oxyhydroxide precipitated from a U^{VI} solution under
491 the solution conditions of our study. Scanning electron microscopy (Fig. 4A) indicates a morphology
492 similar to sodium uranate type U^{VI}-oxyhydroxides, which have been observed to form round or hexagonal
493 plates and rosettes (Buck et al., 2004; Díaz Arocas and Grambow, 1998). Less well-crystallized or
494 agglomerated nanoparticulate material is also evident in the SEM image, which may be unoxidized UO_2
495 (~9% of the initial uraninite is still detected by linear combination fits of the EXAFS spectrum after 72
496 hours of oxidation). Results from pXRD of the solids (Fig. 5) indicate that the UO_2 has been oxidized
497 primarily to Na-compreignacite ($Na_2(UO_2)_6O_4(OH)_6{\cdot}7H_2O$) (Gorman-Lewis et al., 2008). The XRD result
498 is at odds with the measured U concentrations in our study, with the dissolved U concentration lower than
499 the solubility of Na-compreignacite. However, we note that the presence of small amounts of UO_{2+x} (as
500 suggested by the EXAFS and SEM data) may provide a sink for U^{VI} through sorption (Wang et al., 2015),
501 lowering its concentration below the solubility of Na-compreignacite.
502 The EXAFS spectrum (Fig. 3) of the product resulting from 72 hours of U^{IV}-phosphate oxidation
503 is similar to autunite ($Ca(UO_2)_2(PO_4)_2{\cdot}12H_2O$). The same EXAFS spectrum is observed for the solid
504 precipitated from aqueous U^{VI} through the addition of Ca and PO_4 (400 μM each) under the solution
505 conditions of our study (i.e., U^{VI} concentration, buffer, electrolyte, and pH). SEM indicates the formation
506 of a well-defined mineral after oxidation (Fig. 4C), with a morphology consistent with that of autunite
507 (tabular, rectangular appearance) (Anthony et al., 2003). Analysis with SEM-EDX confirms that the solid
508 product contains U and P (Fig. 6), as well as a small amount of Ca (inset, Fig. 6). Sodium is also likely
509 present but is not detected in the SEM-EDX spectra because low-energy x-ray photons are absorbed by
510 the Be window of the detector (Na K_α = 1,040 eV). Results from pXRD of the U^{VI} phase formed (Fig. 5)
511 indicate that the (002) peak of the diffraction pattern is closest to that of meta-natroautunite
512 ($Na_2(UO_2)_2(PO_4)_2{\cdot}8H_2O$). The slight shift of the (002) peak towards the smaller angle/greater d-spacing of

513 Ca-autunite indicates that the interlayer of the U^{VI}-product may contain some calcium, in agreement with
514 the SEM-EDS spectrum and with the solution phase measurements. The pXRD and SEM results are also
515 consistent with geochemical speciation calculations that suggest that Na-(meta)autunite is the predicted
516 solubility-limiting phase in our systems (Fig. 2B).
517
518 **3.2. Effect of calcium, sodium, and phosphate on U^{IV}-oxidation**
519 Phosphate is present in many natural systems and can affect U speciation in several ways. A
520 number of studies indicate that U^{IV} produced in U^{VI} reduction experiments often binds to inorganic
521 phosphate present in the medium or to phosphoryl groups associated with biomass (Alessi et al., 2014b;
522 Bargar et al., 2013; Bernier-Latmani et al., 2010; Boyanov et al., 2011; Fletcher et al., 2010; Sharp et al.,
523 2011; Vecchia et al., 2010). Phosphate also plays a role in remediation strategies relying on the
524 precipitation of U^{VI}-phosphate minerals or as U^{VI} adsorbed/incorporated into Ca-phosphate minerals such
525 as apatite (Arey et al., 1999; Beazley et al., 2007; Fuller et al., 2002; Murakami et al., 2005; Singh et al.,
526 2010). Although sparingly soluble, U^{VI} in phosphate minerals is not inert and can be reduced by metal-
527 reducing bacteria to produce U^{IV}-phosphate minerals (Rui et al., 2013). U-phosphate interactions can also
528 be important in field-scale remediation approaches, as phosphate was a non-negligible component of the
529 emulsified vegetable oils mixture used in a recent bioremediation study (approx. 0.05 wt % $(NH_4)_3PO_4$,
530 equivalent to ~0.7 mM PO_4^{3-} at injection) and could also be a component of the emulsifiers used in such
531 mixtures through hydrolysis of phospholipids such as lecithin (Borden and Lee, 2008; Watson et al.,
532 2013). Therefore, the unknown effect of phosphate on U^{IV} oxidation needs to be assessed in consideration
533 of the potential for remobilization of reduced uranium. Here we have investigated the impact of varying
534 phosphate and calcium concentrations on the oxidation of UO_2 or U^{IV}-phosphate. We hypothesized that
535 uranium oxidation would be slowed by the presence of phosphate and calcium, primary through
536 formation of passivating U^{VI}-phosphate surface layers. As above, we carried out experiments in oxic 5
537 mM MOPS buffer and 15 mM $NaClO_4$ background electrolyte, adjusted to a pH value of 7.0.

538

539 3.2.1. ***Effect of Ca and P on the rate of oxidation.***

540 We compared the oxidation of UO_2 in phosphate-free buffer to the oxidation of UO_2 in the
541 presence of 400 μM Ca^{2+} and PO_4^{3-}. The raw XANES spectra are shown in Fig. EA2. The proportions of
542 U^{IV} over a 72 hour period were obtained from LC fits of the data and are plotted in Fig. 1. It is clear from
543 Fig. 1 that the apparent rate and extent of UO_2 oxidation is decreased in the presence of added calcium
544 and phosphate. The rate constants (k_{obs}) differ by an order of magnitude (Table 1) (k_{obs} = 0.23 h^{-1} vs 0.022
545 h^{-1} with Ca and PO_4).

546 We also compared the rates of U^{IV}-phosphate oxidation in the presence and absence of additional
547 100 or 400 μM Ca and PO_4 (Fig. 1). The raw XANES spectra are shown in Fig.s EA4 and EA5 in the
548 Electronic Annex (EA). Addition of 100 μM Ca/PO_4 results in a rate constant decrease by a factor of 1.8
549 (k_{obs} = 0.077 h^{-1}) relative to the U^{IV}-phosphate system without amendments, whereas addition of 400 μM
550 Ca/PO_4 results in a rate constant decrease by a factor of 2.7 (k_{obs} = 0.044 h^{-1}). Therefore, the relative
551 decrease in the observed oxidation rate constant upon addition of Ca and PO_4 is greater for UO_2 than for
552 U^{IV}-phosphate, with the oxidation rate constants differing by a factor of 1 to 2 between the UO_2 and U^{IV}-
553 phosphate systems with added 400 μM Ca and PO_4.

554 To narrow down whether the decrease in oxidation rates was caused by Ca or PO_4, or by their
555 combined presence, we measured the rate of UO_2 oxidation only in the presence of 400 μM Ca, without
556 phosphate addition. A new batch of UO_2 starting material was used for these experiments, which showed
557 similar oxidation kinetics as the original batch of UO_2 in the absence of additions (Fig. 7). The
558 determined oxidation rate constant for the new UO_2 batch is slightly lower (k_{obs} = 0.087 h^{-1}, Table 1),
559 possibly due to the coarser sampling of the initial kinetics. Addition of 400 μM Ca to the UO_2 suspension
560 had no effect on the rate or extent of oxidation over the course of the experiment (Fig. 7). Our observation
561 that Ca has little impact on U^{IV} oxidation is in contrast with previous reports that Ca-containing U^{VI}
562 minerals, including Ca-U^{VI} carbonates and silicates, form on the surface of UO_2 and inhibit its oxidative

563 dissolution (Cerrato et al., 2012; Giammar et al., 2012; Santos et al., 2006a). It is therefore likely that Ca
564 affects U^{IV} oxidation only when present together with carbonate and/or silicate and that the lack of large
565 quantities of carbonate (dissolved HCO_3^- ~ 100 μM) or silicate in our system precluded the formation of
566 surface precipitates.

567 We also tested the impact of PO_4 addition on UO_2 oxidation in the absence of Ca. Addition of 400
568 μM PO_4 to the UO_2 suspension slowed the initial rate of oxidation (k_{obs} = 0.068 h^{-1}), but increased the
569 extent of oxidation after 38 hours over that of the UO_2 alone and UO_2 + Ca reactors. The slight inhibition
570 of the oxidation rate initially may be due to precipitation of U^{VI}-phosphate surface layers (Shoesmith et
571 al., 1988), which have been observed to partially passivate the UO_2 surface toward oxidation (Shoesmith
572 et al., 1988). However, under conditions similar to our experiment (neutral pH and 10 mM $NaClO_4$
573 electrolyte), phosphate increased the rate of UO_2 dissolution above that observed for similar
574 concentrations of carbonate by 1.5 orders of magnitude (Rey et al., 2008). It is possible that in our study
575 passivation is balanced by PO_4-promoted dissolution and subsequent re-precipitation as U^{VI}-phosphate.
576 Overall, the data suggest that addition of Ca and PO_4 together is more effective in decreasing the rate of
577 U^{IV} oxidation in suspensions of UO_2 than addition of either Ca or PO_4 alone.
578

579 **3.2.2. Effect of Ca and P on solution dynamics**

580 Measurable concentrations of dissolved U were present in systems without added Ca and PO_4
581 (Table 2). Addition of Ca and PO_4 to suspensions of UO_2 or U^{IV}-phosphate results in lower dissolved
582 uranium concentrations down to the detection limit of ~17 nM U. The decrease in U solubility is
583 consistent with thermodynamic calculations, which show 2–3 orders of magnitude decrease in solubility
584 of Ca-autunite and Na-autunite when excess Ca or Na and PO_4 are present (Fig. 2B). Furthermore,
585 solution measurements indicate that some of the added Ca and PO_4 is removed from solution during the
586 oxidation process (Table 2). As discussed further below, the uptake of these species is consistent with the
587 solid products formed.

588

589 **3.2.3. Effect of Ca and P on the products of U^{IV} oxidation**

590 Addition of calcium and phosphate to reactors with UO_2 as the starting U^{IV} phase results in a
591 significant change in the oxidized U^{VI} product relative to UO_2 alone. In the absence of Ca and PO_4 the
592 EXAFS spectra of the solids after 72 hours of oxidation closely match the spectra of U^{VI}-oxyhydroxides
593 (Fig. 3). The product of UO_2 oxidation in the presence of 400 μM Ca is the same as that without added
594 Ca, and is consistent with the observed similarity in oxidation kinetics. In the presence of 400 μM Ca and
595 PO_4 during UO_2 oxidation, the resulting spectra match those of precipitated U^{VI}-phosphate and autunite.

596 The EXAFS results are corroborated by SEM images of the oxidized UO_2 products, where a
597 significantly different morphology is seen in the absence (Fig. 4A) and presence of Ca and PO_4 (Fig. 4B).
598 The U^{VI} product obtained in the absence of Ca/PO_4 has morphology similar to that of schoepite and other
599 uranyl oxy-hydroxides, whereas a rectangular platy morphology typical of autunite-group minerals is
600 observed in reactors with added Ca and PO_4 (Wellman et al., 2006). The pXRD results (Fig. 5) suggest
601 that a mixture of two phases exists in the system with Ca/PO_4, as judged by the split (002) peak near
602 10°2θ that is consistent with both meta-natroautunite or chernikovite and a phase similar to Ca-autunite.
603 We suspect the monovalent autunite in our study is (meta-)natroautunite, rather than chernikovite, given
604 that the concentration of Na^+ is five orders of magnitude greater than that of H_3O^+. Incorporation of Ca
605 into the final products is corroborated by the SEM-EDS spectrum, where the Ca K_α fluorescence line is
606 observed (Fig. 6, inset). Overall, the EXAFS, pXRD, and SEM-EDS data suggest that the U^{VI} product
607 from UO_2 oxidation in the presence of Ca and PO_4 is a mixture of Na- and Ca-autunites.

608 The products of U^{IV}-phosphate oxidation after 72 hours, both in systems with and without
609 addition of 100 or 400 μM Ca and PO_4, have the same EXAFS spectrum that corresponds to a U^{VI}-
610 phosphate material (Fig. 3). The latter indicates that the U^{VI}-phosphate coordination in the autunite layer
611 is the same regardless of the presence or absence of excess Ca/PO_4. There are minor differences in the
612 SEM images of the U^{IV}-phosphate oxidation products produced in the absence and presence of added Ca

and PO_4 (Fig.s 4C, 4D, and 4E); however, overall the particles have a morphology consistent with sheets and plates of autunite minerals. In the absence of added Ca/PO_4, the particles appear slightly larger and less aggregated. Diffraction lines for the U^{VI}-phosphate product in the reactors without addition of Ca and PO_4 are narrower than lines for the products formed with 100 or 400 μM Ca and PO_4, also suggesting larger particle size in the absence of Ca and PO_4. Elemental analysis using SEM-EDX (Fig. 6) shows that the oxidation products obtained in the presence of increasing aqueous Ca and PO_4 concentrations contain the same amount of U and PO_4, but increasing amounts of incorporated or adsorbed Ca. The increase in Ca content in the oxidation products is corroborated by the pXRD data (Fig. 5), which show a progressive shift in the position of the (002) peak (~10 deg 2θ) from that of metanatroautunite or chernikovite to that of Ca-autunite. In combination, the SEM-EDX and pXRD data suggest a progressive incorporation of Ca into the autunite interlayer during U^{IV}-phosphate oxidation at elevated Ca concentrations.

3.3. Mechanism of U^{IV} oxidation in the presence of Ca, PO_4, and Na

The data presented to this point indicate that the oxidation rates of UO_2 and of U^{IV}-phosphate are slowed most significantly by the combined addition of Ca and PO_4. Potential explanations for the effect of Ca and PO_4 include (i) influence on the solubility of the starting U^{IV} phases, (ii) influence on the thermodynamic driving force for oxidation to the end products, (iii) changes in aggregate status leading to reduced reactive surface area or O_2 diffusion into flocs, or (iv) passivation/encapsulation of the U^{IV}-surface by Ca-PO_4 or Ca/U^{VI}-PO_4 products formed during oxidation. Below we discuss each of these mechanisms in the context of the current results and the data available in the literature.

3.3.1. U^{IV} solubility and thermodynamic driving force

We can discount a role for differences in solubility driving the observed differences in oxidation rates of the U^{IV} phases in buffer alone versus Ca and PO_4 containing solution (Table 1). A dependence of oxidation rate on solubility would imply a mechanism whereby the dissolved U^{IV} species are oxidized to

638 U^{VI}. However, our U concentration measurements in the anoxic controls (samples at time 0 hours,
639 Table 2) indicate dissolved U is at or near the detection limit of ~17 nM of the KPA method we used, and
640 accounts for <0.02% of the total uranium in the system. This suggests that oxidation of U^{IV} is likely
641 dominated by surface-mediated processes. Support for surface-controlled U^{IV} oxidation also comes from
642 studies showing that oxidized U products (U^{V} and U^{VI}) accumulate on the UO_2 surface, as well as from
643 studies that have demonstrated higher oxidant reduction rates with increasing U^{IV} solid surface area
644 (Ekeroth and Jonsson, 2003; Hossain et al., 2006; Shoesmith et al., 1989; Sunder et al., 1991; Ulrich et
645 al., 2009).

646 Another potential factor influencing oxidation rate is the thermodynamic driving force for
647 oxidation to different U^{VI} products, which may be the reason for the observed slower rate of UO_2
648 oxidation in our systems with added Ca/PO_4 (end product autunite) relative to the systems without Ca/PO_4
649 (end product schoepite or Na-compreignacite). Thermodynamic calculations (details in EA) suggest that
650 under the conditions of this study UO_2 oxidation to autunite is less favorable (-379 kJ/mol) than oxidation
651 to Na-compregnacite (-1,009 kJ/mol). However, the calculation does not take into account any activation
652 energy barriers that could limit the rate of reaction. Although the difference in energy suggests a larger
653 driving force for oxidation to Na-compregnacite, the inability to account for the activation barrier
654 precludes a conclusion on the cause for the larger oxidation rate constant without Ca and PO_4. Therefore,
655 the magnitude of the energy difference between the two reactions cannot be inferred to be the cause of the
656 differences in oxidation rate with and without the presence of Ca and PO_4.
657

658 **3.3.2. Aggregation of UO_2 and U^{IV}-phosphate**

659 Because the thermodynamic driving force or solubility considerations above were inconclusive,
660 we tested the hypothesis that Ca and PO_4 cause different aggregation in the UO_2 and U^{IV}-phosphate
661 suspensions. Aggregation is known to affect the reactivity of nanoparticulate oxides (Cwiertny et al.,
662 2008; Lanzl et al., 2012; Stemig et al., 2014). In our system, aggregation could have limited the diffusion

663 of oxygen between the particles or could have occluded some of the surface sites. To test for aggregation,
664 we compared the sedimentation rates of UO_2 and U^{IV}-phosphate suspensions in the absence and presence
665 of 400 μM Ca and PO_4. A decrease in absorbance was interpreted as a combined measure of aggregation
666 and sedimentation, assuming that absorbance was due predominantly to scatter (Cwiertny et al., 2008;
667 Lanzl et al., 2012). The results from this experiment (Fig. 8) suggest that addition of Ca and PO_4 has an
668 impact on aggregation in suspensions of UO_2, but does not alter the sedimentation rates of the U^{IV}-
669 phosphate particles used in the study. We obtained the same absorbance profiles for repeat settling after
670 resuspension of both the UO_2 and U^{IV}-PO_4 suspensions, indicating that the particle size distributions are
671 stable and that any flocculation is reversible.
672 While the initial settling rates for UO_2 are similar with and without amendments, over time the
673 suspension with added Ca and PO_4 settles faster. Homogeneous precipitation of Ca-PO_4 particles can be
674 excluded as the reason for increased sedimentation because there was no increase in light absorbance in
675 400 μM Ca and PO_4 containing solutions relative to a buffer-only control. It is possible that Ca and/or
676 PO_4 caused compensation of surface charge or surface-catalyzed formation of Ca-PO_4, leading to particle
677 aggregation. The resulting decrease in exposed surface area may be one reason for the decreased
678 oxidation rate in the presence of Ca and PO_4 relative to the system without amendments.
679
680 **3.3.3. Surface passivation of UO_2 and U^{IV}-phosphate by Ca and PO_4**
681 Based on several studies suggesting that passivation layers influence the oxidation of U^{IV} in UO_2
682 (Roth and Jonsson, 2008; Santos et al., 2006b; Shoesmith et al., 1988, 1989) and the subsequent release of
683 U^{VI} (Cerrato et al., 2012; Giammar et al., 2012), we hypothesized that Ca and PO_4 promoted the
684 formation of a surface layer during UO_2 oxidation and resulted in the observed slower U^{IV} oxidation rates.
685 In an attempt to dissolve U^{VI} from the surface layer, we oxidized UO_2 in the presence of 400 μM Ca and
686 PO_4 for 10 hours, followed by extraction of the solids in anoxic 100 mM $NaHCO_3$ (pH 8.2). The extracted
687 solids were used as starting material in a new oxidation experiment without added Ca or PO_4 (i.e.,

688 resuspended to the same U concentrations but in a Ca- and PO_4-free buffer solution saturated with O_2
689 from air). The valence state of U over time from pre- and post-extraction solids are compared in Fig. 9 to
690 a Ca- and PO_4-free UO_2 oxidation experiment for this new batch of UO_2.

691 The data in Fig. 9 show the same trend as the data in Fig. 1, namely that UO_2 with 400 µM Ca
692 and PO_4 (red circles) oxidizes more slowly and less extensively than UO_2 alone (blue squares). We also
693 find that bicarbonate extraction of the UO_2 solids that were oxidized for 10 hours in the presence of Ca
694 and PO_4 did not remove all of the oxidized uranium, as the fit of the XANES data from the pre-extraction
695 and post-extraction solids indicate similar U^{IV} content (67% vs. 72% U^{IV}/U_{total}, respectively). Solution
696 measurements corroborate the XANES data (Table 3), with extraction of the UO_2 + Ca and PO_4 solids
697 removing only 12% (12 µM U_{total}) of the U_{total} from the suspension, as well as 6.9 µM Ca and 20 µM
698 PO_4. Control experiments indicate that autunite is more soluble in 100 mM bicarbonate than
699 hydroxyapatite (91% vs. 28% extraction of PO_4), suggesting that bicarbonate dissolves more autunite than
700 calcium phosphate phases, which together with the observed ratios of U, Ca, and PO_4 in the extract,
701 suggest dissolution of an autunite layer on the UO_2 solids. Digestion of the post-extraction solids in oxic
702 HNO_3 showed no detectable calcium or phosphate, suggesting that Ca and PO_4 were largely removed and
703 due to dilution were below the detection limit of ICP-OES (but not x-ray fluorescence as seen in Fig. 10)
704 in the extracted layer. Subsequent oxidation of the UO_2 solids after extraction follows a trend that is
705 similar to the oxidation of the original UO_2 solids in systems without added Ca and PO_4 (Fig. 9, green
706 circles). These data indicate that bicarbonate extraction removed a Ca, U^{IV}, and PO_4-containing
707 passivation layer and that the lack of Ca and PO_4 in the post-extraction solution prevented a new layer
708 from forming.

709 Our observation that 100 mM bicarbonate extraction does not remove all of the oxidized U
710 present in the UO_2 nanoparticle is notable. Previous research indicates that 100 mM HCO_3^- solutions
711 typically remove $UO_{2.33}$ surface layers on bulk UO_2 minerals through UO_2^{2+} complexation (Shoesmith,
712 2000), resulting in stoichiometric UO_2 in the 5–10 nm surface layer as determined by x-ray photoelectron

713 spectroscopy. In contrast, the XANES results here are consistent with the oxidation of UO_2 nanoparticles
714 resulting in conversion of the whole 3.5 nm particle to UO_{2+x}, in which the oxidized U^{V}/U^{VI} species are
715 relatively stable to bicarbonate extraction.

716 We also sought spectroscopic identification of the passivation layer using Ca K-edge XAS. The
717 XANES spectra from the UO_2 + 400 μM Ca and PO_4 system after 10 hours of oxidation are shown at the
718 top of Fig. 10. The XANES spectra of the oxidized pre-extraction solids, the oxidized extracted solids,
719 and the UO_2 + Ca and PO_4 anoxic control are nearly identical and indicate the same Ca speciation in all
720 three systems. When compared to those of hydroxyapatite, calcite ($CaCO_3$), synthetic Ca-autunite, and a 1
721 M solution of $CaCl_2$, the spectra are most similar to those from the aqueous Ca^{2+} and the autunite
722 standards. The EXAFS data of the UO_2 samples are also similar to those of the aqueous Ca^{2+} and autunite
723 standards, but differ from the spectra of hydroxyapatite and calcite (Fig. 11). These results confirm the
724 lack of significant hydroxyapatite or calcite precipitation in the system. The Fourier transforms of the data
725 (Fig. 11B) lack features from outer coordination shells, similar to the Ca-autunite and the aqueous $CaCl_2$
726 solution standards. The lack of outer-shell peaks in these standards is due to the single-shell coordination
727 of Ca in the inter-layer space of autunite and the disordered outer-hydration shell in dissolved Ca. The
728 lack of second-shell coordination features in the oxidized UO_2 samples suggests that Ca is associated with
729 the solids via outer-sphere complexation or by incorporation in the inter-layer space of a mineral (as in
730 autunite). Taken together with the bicarbonate extraction results (showing the presence of U, Ca, and PO_4
731 in the dissolved layer), the Ca-edge spectroscopy results indicate the formation of a passivation layer with
732 a structure similar to that of autunite.

733 In summary, our results indicate that the presence of calcium and phosphate in UO_2 suspensions
734 induces a small change in particle aggregation and causes the formation of an autunite surface layer
735 during oxidation. The extraction data and Ca XAS spectra suggest that a Ca-U^{VI}-PO_4 surface layer is
736 formed. Removal of the U^{VI}-PO_4 layer returns the reactivity of UO_2 to that of UO_2 suspensions without
737 added Ca and PO_4. The results suggest that U^{VI}-PO_4 surface layers passivate nanoparticulate UO_2 and

738 slow the rate of U^{IV} oxidation, consistent with previous observations of passivation of bulk UO_2
739 electrodes in PO_4-containing solutions (Shoesmith et al., 1988). As with bulk UO_2, our results indicate
740 that U^{VI}-PO_4 layers are quite thin, comprising 5 to 12% of the total U present in the suspensions.
741 However, such layers slow down the rate of UO_2 oxidation and decrease the solubility of U^{VI} through
742 formation of U^{VI}-PO_4 minerals.
743
744 **4. Implications for Uranium Dynamics and Transport Modelling**
745 The results of this work suggest that two of the U^{IV} species expected to form under reducing
746 conditions in uranium contaminated sediments—nanoparticulate UO_2 and (Ca-)U^{IV}-phosphate—are likely
747 to be oxidized by dissolved oxygen (O_2) at rates that are within an order of magnitude of each other. The
748 relative oxidation rates determined here in systems at neutral pH and low bicarbonate content are
749 consistent with the relative rates of oxidation of these two materials observed in recent work (Cerrato et
750 al., 2013); however, the surface-normalized rates determined here for nanoparticulate UO_2 are greater by
751 approximately one to two orders of magnitude relative to those measured for bulk UO_2 (Roth and
752 Jonsson, 2008). The difference in our study is likely due to accounting for oxidized U remaining inside
753 the solid phase, the stability of which will depend on the solution conditions. The oxidation rate constants
754 will be useful in building comprehensive geochemical models for U fate and transport in the subsurface
755 (Li et al., 2009; Yabusaki et al., 2007b). To date, development of numerical groundwater models has
756 progressed to the point of including the kinetics of U reductive immobilization (e.g., (Li et al., 2010; Li et
757 al., 2009; Yabusaki et al., 2007a). Future model development will aim to predict U^{IV} oxidation and
758 mobilization on a more holistic level, coupling it to biological processes such as endogenous decay of
759 biomass, respiration scavenging of O_2 and production of CO_2, and abiotic reactions such as FeS oxygen
760 scavenging (Bi and Hayes, 2013; Bi et al., 2013). Knowledge of the oxidation rates of relevant U^{IV}
761 species will be essential in estimating the importance of different O_2-consuming reactions in realistic
762 systems.

763 Furthermore, our study shows that at low concentrations of bicarbonate and sodium, the oxidation
764 of UO_2 leads to the formation of low-solubility sodium uranate type minerals such as clarkeite or Na-
765 compreignacite. This finding may have implications for U speciation at several uranium contaminated
766 sites where sodium concentrations are similar to those in our study (Revil et al., 2013; Zachara et al.,
767 2013). Knowledge of the oxidized phase identity under various conditions is important in estimating the
768 mobility of U following reductive immobilization.
769 Our results also indicate that the presence of phosphate can mitigate the oxidative dissolution of
770 U^{IV}. Phosphate is now established as playing a significant role in binding U^{IV} during U^{VI} reduction
771 (Bargar et al., 2013; Bernier-Latmani et al., 2010; Boyanov et al., 2011; Rui et al., 2013; Sharp et al.,
772 2011; Sivaswamy et al., 2011; Veeramani et al., 2011) and will likely be a non-negligible component of
773 many bioremediation influents (e.g., the emulsified vegetable oils used in a recent field-scale
774 bioremediation study contained 0.05 wt% $(NH_4)_3PO_4$ (Watson et al., 2013). In our study, the combination
775 of calcium and phosphate slowed down the rate of UO_2 and U^{IV}-phosphate oxidation by up to an order of
776 magnitude. However, the oxidation rates of U^{IV} were still fast enough to account for complete oxidation
777 of U^{IV} within days under fully oxygenated conditions. Under the conditions of our study, we observed the
778 formation of Na-autunite rather than Ca-autunite phases after oxidation of UO_2 and Ca-U^{IV}-phosphate.
779 The lower solubility of Na-autunite relative to Ca-autunite maintained lower concentrations of dissolved
780 U^{VI} in our system. Our work here, along with another recent study (Mehta et al., 2014), highlights the
781 overall importance of dissolved Na^+ in mitigating the solubility of U^{VI} in the presence or absence of
782 phosphate and indicates that solution conditions (e.g. dissolved cations, phosphate, and carbonate) will
783 have a significant impact on the U^{VI} products formed from U^{IV} oxidation. The combined effects of alkali
784 metals (Na^+, K^+) as well as carbonate on U^{VI} solubility should be included in future U^{VI} reactive transport
785 models.
786 Finally, our study provides mechanistic insight on the U^{IV} oxidation process, which informs how
787 to control U^{IV} oxidation and which phases to consider in modelling the fate and transport of U. The

observed formation of U^{IV}-Ca-PO_4 surface layers during oxidation of UO_2 appears to passivate the surface from further oxidation and suggests that long-term immobilization of subsurface U contamination might be best achieved through a defense-in-depth methodology that combines reductive immobilization with concomitant additions of phosphate and calcium.

Acknowledgements

We thank Edward O'Loughlin for insightful discussions and Carolyn Steele for editing the final version of the manuscript. This research is part of the Subsurface Science Scientific Focus Area at Argonne National Laboratory, which is supported by the DOE Subsurface Biogeochemical Research Program, Office of Biological and Environmental Research, Office of Science. Use of the Electron Microscopy Center at Argonne and the Advanced Photon Source was supported by the U.S. Department of Energy, Office of Science, Office of Basic Energy Sciences. MRCAT/EnviroCAT operations are supported by DOE and the MRCAT/EnviroCAT member institutions. All work at Argonne was under Contract DE-AC02-06CH11357.

804 **References**

805 Alessi, D.S., Lezama-Pacheco, J.S., Janot, N., Suvorova, E.I., Cerrato, J.M., Giammar, D.E., Davis, J.A.,
806 Fox, P.M., Williams, K.H., Long, P.E., Handley, K.M., Bernier-Latmani, R., Bargar, J.R., 2014a.
807 Speciation and Reactivity of Uranium Products Formed during in Situ Bioremediation in a Shallow
808 Alluvial Aquifer. Environmental Science & Technology. 48, 12842-12850.

809 Alessi, D.S., Lezama-Pacheco, J.S., Stubbs, J.E., Janousch, M., Bargar, J.R., Persson, P., Bernier-
810 Latmani, R., 2014b. The product of microbial uranium reduction includes multiple species with U(IV)–
811 phosphate coordination. Geochimica et Cosmochimica Acta. 131, 115-127.

812 Alessi, D.S., Uster, B., Veeramani, H., Suvorova, E.I., Lezama-Pacheco, J.S., Stubbs, J.E., Bargar, J.R.,
813 Bernier-Latmani, R., 2012. Quantitative separation of monomeric U(IV) from UO_2 in products of U(VI)
814 reduction. Environmental Science & Technology. 46, 6150-6157.

815 Anthony, J.W., Bideaux, R.A., Bladh, K.W., Nichols, M.C., 2003. Handbook of Mineralogy.
816 Mineralogical Society of America, Chantilly, VA, USA.

817 Arey, J.S., Seaman, J.C., Bertsch, P.M., 1999. Immobilization of uranium in contaminated sediments by
818 hydroxyapatite addition. Environmental science & technology. 33, 337-342.

819 Bargar, J.R., Reitmeyer, R., Davis, J.A., 1999. Spectroscopic Confirmation of Uranium (VI) - Carbonate
820 Adsorption Complexes on Hematite. Environmental Science and Technology. 33, 2481-2484.

821 Bargar, J.R., Williams, K.H., Campbell, K.M., Long, P.E., Stubbs, J.E., Suvorova, E.I., Lezama-Pacheco,
822 J.S., Alessi, D.S., Stylo, M., Webb, S.M., Davis, J.A., Giammar, D.E., Blue, L.Y., Bernier-Latmani, R.,
823 2013. Uranium redox transition pathways in acetate-amended sediments. Proceedings of the National
824 Academy of Sciences. 110, 4506-4511.

825 Bau, S., Witschger, O., Gensdarmes, F., Rastoix, O., Thomas, D., 2010. A TEM-based method as an
826 alternative to the BET method for measuring off-line the specific surface area of nanoaerosols. Powder
827 Technology. 200, 190-201.

828 Beazley, M.J., Martinez, R.J., Sobecky, P.A., Webb, S.M., Taillefert, M., 2007. Uranium
829 biomineralization as a result of bacterial phosphatase activity: insights from bacterial isolates from a
830 contaminated subsurface. Environmental science & technology. 41, 5701-5707.

831 Bernier-Latmani, R., Veeramani, H., Vecchia, E.D., Junier, P., Lezama-Pacheco, J.S., Suvorova, E.I.,
832 Sharp, J.O., Wigginton, N.S., Bargar, J.R., 2010. Non-uraninite Products of Microbial U(VI) Reduction.
833 Environmental Science & Technology. 44, 9456-9462.

834 Bi, Y., Hayes, K.F., 2013. Nano-FeS inhibits UO_2 reoxidation under varied oxic conditions.
835 Environmental science & technology.

836 Bi, Y., Hyun, S.P., Kukkadapu, R.K., Hayes, K.F., 2013. Oxidative dissolution of UO_2 in a simulated
837 groundwater containing synthetic nanocrystalline mackinawite. Geochimica et Cosmochimica Acta. 102,
838 175-190.

839 Borden, R.C., Lee, M.D., 2008. Method for remediation of aquifers. Google Patents.

840 Boyanov, M.I., Fletcher, K.E., Kwon, M.J., Rui, X., O'Loughlin, E.J., Löffler, F.E., Kemner, K.M., 2011.
841 Solution and microbial controls on the formation of reduced U(IV) species. Environmental Science &
842 Technology. 45, 8336-8344.

843 Brooks, S.C., Fredericksson, J.K., Carroll, S.L., Kennedy, D.W., Zachara, J.M., Plymale, A., Kelly, S.D.,
844 Kemner, K.M., Fendorf, S., 2003. Inhibition of Bacterial U(VI) Reduction by Calcium. Environmental
845 Science and Technology. 37, 1850-1858.

846 Buck, B.J., Brock, A.L., Johnson, W.H., Ulery, A.L., 2004. Corrosion of depleted uranium in an arid
847 environment: Soil-geomorphology, SEM/EDS, XRD, and electron microprobe analyses. Soil & Sediment
848 Contamination. 13, 545-561.

849 Burns, P.C., Ewing, R.C., Navrotsky, A., 2012. Nuclear Fuel in a Reactor Accident. Science. 335, 1184-
850 1188.

851 Campbell, K.M., Veeramani, H., Ulrich, K.-U., Blue, L.Y., Giammar, D.E., Bernier-Latmani, R., Stubbs,
852 J.E., Suvorova, E., Yabusaki, S., Lezama-Pacheco, J.S., Mehta, A., Long, P.E., Bargar, J.R., 2011.
853 Oxidative Dissolution of Biogenic Uraninite in Groundwater at Old Rifle, CO. Environmental Science &
854 Technology. 45, 8748-8754.

855 Cerrato, J.M., Ashner, M.N., Alessi, D.S., Lezama-Pacheco, J.S., Bernier-Latmani, R., Bargar, J.R.,
856 Giammar, D.E., 2013. Relative Reactivity of Biogenic and Chemogenic Uraninite and Biogenic
857 Noncrystalline U(IV). Environmental Science and Technology. 47, 9756-9763.

858 Cerrato, J.M., Barrows, C.J., Blue, L.Y., Lezama-Pacheco, J.S., Bargar, J.R., Giammar, D.E., 2012. Effect
859 of Ca^{2+} and Zn^{2+} on UO_2 Dissolution Rates. Environmental Science and Technology. 46, 2731-2737.

860 Cwiertny, D.M., Handler, R.M., Schaefer, M.V., Grassian, V.H., Scherer, M.M., 2008. Interpreting
861 nanoscale size-effects in aggregated Fe-oxide suspensions: reaction of Fe(II) with goethite. Geochimica
862 Et Cosmochimica Acta. 72, 1365-1380.

863 Díaz Arocas, P., Grambow, B., 1998. Solid-liquid Phase Equilibria of U(VI) in NaCl Solutions.
864 Geochimica et Cosmochimica Acta. 62, 245-263.

865 Ekeroth, E., Jonsson, M., 2003. Oxidation of UO_2 by radiolytic oxidants. Journal of Nuclear Materials.
866 322, 242-248.

867 Fletcher, K.E., Boyanov, M.I., Thomas, S.H., Wu, Q.Z., Kemner, K.M., Loffler, F.E., 2010. U(VI)
868 reduction to mononuclear U(IV) by *Desulfitobacterium* species. Environmental Science & Technology.
869 44, 4705-4709.

870 Fuller, C., Bargar, J., Davis, J., Piana, M., 2002. Mechanisms of uranium interactions with
871 hydroxyapatite: Implications for groundwater remediation. Environmental Science and Technology. 36,
872 158-165.

873 Giammar, D.E., Cerrato, J.M., Mehta, V., Wang, Z., Wang, Y., Pepping, T.J., Ulrich, K.-U., Lezama-
874 Pacheco, J.S., Bargar, J.R., 2012. Effect of diffusive transport limitations on UO_2 dissolution. Water
875 Research. 46, 6023-6032.

876 Giammar, D.E., Hering, J.G., 2004. Influence of dissolved sodium and cesium on uranyl oxide hydrate
877 solubility. Environmental Science & Technology. 38, 171-179.

878 Ginder-Vogel, M., Criddle, C.S., Fendorf, S., 2006. Thermodynamic constraints on the oxidation of
879 biogenic UO2 by Fe(III) (hydr) oxides. Environmental Science & Technology. 40, 3544-3550.

880 Goldstein, J., 2011. How to build a better sepulcher: Lessons from New Mexico's Waste Isolation Pilot
881 Plant. Bulletin of the Atomic Scientists. 67, 77-88.

882 Gorman-Lewis, D., Fein, J.B., Burns, P.C., Szymanowski, J.E.S., Converse, J., 2008. Solubility
883 measurements of the uranyl oxide hydrate phases metaschoepite, compreignacite, Na–compreignacite,
884 becquerelite, and clarkeite. The Journal of Chemical Thermodynamics. 40, 980-990.

885 Hossain, M.M., Ekeroth, E., Jonsson, M., 2006. Effects of on the kinetics of UO_2 oxidation by H_2O_2.
886 Journal of Nuclear Materials. 358, 202-208.

887 Jang, J.-H., Dempsey, B.A., Burgos, W.D., 2006. Solubility of schoepite: Comparison and selection of
888 complexation constants for U(VI). Water Research. 40, 2738-2746.

889 Kelly, S.D., Kemner, K.M., Fein, J.B., Fowle, D.A., Boyanov, M.I., Bunker, B.A., Yee, N., 2002. X-ray
890 absorption fine structure determination of pH-dependent U-bacterial cell wall interactions. Geochimica Et
891 Cosmochimica Acta. 66, 3855-3871.

892 Kropf, A.J., Katsoudas, J., Chattopadhyay, S., Shibata, T., Lang, E.A., Zyryanov, V.N., Ravel, B.,
893 McIvor, K., Kemner, K.M., Scheckel, K.G., Bare, S.R., Terry, J., Kelly, S.D., Bunker, B.A., Segre, C.U.,
894 2010. The new MRCAT (Sector 10) bending magnet beamline at the Advanced Photon Source. AIP
895 Conference Proceedings. 1234, 299-302.

896 Lanzl, C.A., Baltrusaitis, J., Cwiertny, D.M., 2012. Dissolution of Hematite Nanoparticle Aggregates:
897 Influence of Primary Particle Size, Dissolution Mechanism, and Solution pH. Langmuir. 28, 15797-
898 15808.

899 Latta, D., Mishra, B., Cook, R.E., Kemner, K.M., Boyanov, M.I., 2014. Stable U (IV) complexes form at
900 high-affinity mineral surface sites. Environmental science & technology.

901 Li, D., Kaplan, D.I., Chang, H.-S., Seaman, J.C., Jaffé, P.R., Koster van Groos, P., Scheckel, K.G., Segre,
902 C.U., Chen, N., Jiang, D.-T., Newville, M., Lanzirotti, A., 2015. Spectroscopic Evidence of Uranium
903 Immobilization in Acidic Wetlands by Natural Organic Matter and Plant Roots. Environmental Science &
904 Technology. 49, 2823-2832.

905 Li, L., Steefel, C.I., Kowalsky, M.B., Englert, A., Hubbard, S.S., 2010. Effects of physical and
906 geochemical heterogeneities on mineral transformation and biomass accumulation during biostimulation
907 experiments at Rifle, Colorado. Journal of contaminant hydrology. 112, 45-63.

908 Li, L., Steefel, C.I., Williams, K.H., Wilkins, M.J., Hubbard, S.S., 2009. Mineral Transformation and
909 Biomass Accumulation Associated With Uranium Bioremediation at Rifle, Colorado. Environmental
910 Science and Technology. 43, 5429-5435.

911 Long, P.E., Williams, K.H., Davis, J.A., Fox, P.M., Wilkins, M.J., Yabusaki, S.B., Fang, Y., Waichler,
912 S.R., Berman, E.S.F., Gupta, M., Chandler, D.P., Murray, C., Peacock, A.D., Giloteaux, L., Handley,
913 K.M., Lovley, D.R., Banfield, J.F., 2015. Bicarbonate impact on U(VI) bioreduction in a shallow alluvial
914 aquifer. Geochimica et Cosmochimica Acta. 150, 106-124.

915 Mehta, V.S., Maillot, F., Wang, Z., Catalano, J.G., Giammar, D.E., 2014. Effect of co-solutes on the
916 products and solubility of uranium(VI) precipitated with phosphate. Chemical Geology. 364, 66-75.

917 Murakami, T., Sato, T., Ohnuki, T., Isobe, H., 2005. Field evidence for uranium nanocrystallization and
918 its implications for uranium transport. Chemical geology. 221, 117-126.

919 Newsome, L., Morris, K., Lloyd, J.R., 2014. The biogeochemistry and bioremediation of uranium and
920 other priority radionuclides. Chemical Geology. 363, 164-184.

921 Pierce, E.M., Icenhower, J.P., Serne, R.J., Catalano, J.G., 2005. Experimental determination of UO_2(cr)
922 dissolution kinetics: Effects of solution saturation state and pH. Journal of nuclear materials. 345, 206-
923 218.

924 Ravel, B., Newville, M., 2005. ATHENA, ARTEMIS, HEPHAESTUS: data analysis for X-ray
925 absorption spectroscopy using IFEFFIT. Journal of Synchrotron Radiation. 12, 537-541.

926 Revil, A., Wu, Y., Karaoulis, M., Hubbard, S.S., Watson, D.B., Eppehimer, J.D., 2013. Geochemical and
927 geophysical responses during the infiltration of fresh water into the contaminated saprolite of the Oak
928 Ridge Integrated Field Research Challenge site, Tennessee. Water Resources Research. 49, 4952-4970.

929 Rey, A., Giménez, J., Casas, I., Clarens, F., de Pablo, J., 2008. Secondary phase formation on UO2 in
930 phosphate media. Applied Geochemistry. 23, 2249-2255.

931 Roth, O., Jonsson, M., 2008. Oxidation of UO2 (s) in aqueous solution. Central European Journal of
932 Chemistry. 6, 1-14.

933 Rui, X., Kwon, M.J., O'Loughlin, E.J., Dunham-Cheatham, S., Fein, J.B., Bunker, B., Kemner, K.M.,
934 Boyanov, M.I., 2013. Bioreduction of Hydrogen Uranyl Phosphate: Mechanisms and U(IV) Products.
935 Environmental Science and Technology. 47, 5668-5678.

936 Santos, B.G., Noël, J.J., Shoesmith, D.W., 2006a. The influence of calcium ions on the development of
937 acidity in corrosion product deposits on SIMFUEL, UO2. Journal of Nuclear Materials. 350, 320-331.

938 Santos, B.G., Noël, J.J., Shoesmith, D.W., 2006b. The influence of silicate on the development of acidity
939 in corrosion product deposits on SIMFUEL (UO_2). Corrosion Science. 48, 3852-3868.

940 Segre, C.U., Leyarovska, N.E., Chapman, L.D., Lavender, W.M., Plag, P.W., King, A.S., Kropf, A.J.,
941 Bunker, B.A., Kemner, K.M., Dutta, P., Duran, R.S., Kaduk, J., 2000. The MRCAT insertion device
942 beamline at the Advanced Photon Source. AIP Conference Proceedings. 521, 419-422.

943 Sharp, J.O., Lezama-Pacheco, J.S., Schofield, E.J., Junier, P., Ulrich, K.U., Chinni, S., Veeramani, H.,
944 Margot-Roquier, C., Webb, S.M., Tebo, B.M., Giammar, D.E., Bargar, J.R., Bernier-Latmani, R., 2011.
945 Uranium speciation and stability after reductive immobilization in aquifer sediments. Geochimica et
946 Cosmochimica Acta. 75, 6497-6510.

947 Shoesmith, D., 2000. Fuel corrosion processes under waste disposal conditions. Journal of Nuclear
948 Materials. 282, 1-31.

949 Shoesmith, D.W., Sunder, S., Bailey, M.G., Wallace, G.J., 1988. Anodic-oxidation of UO_2. 5.
950 Electrochemical and X-ray photoelectron spectroscopic studies of film-growth and dissolution in
951 phosphate-containing solutions. Canadian Journal of Chemistry. 66, 259-265.

Shoesmith, D.W., Sunder, S., Bailey, M.G., Wallace, G.J., 1989. The corrosion of nuclear fuel (UO_2) in oxygenated solutions. Corrosion Science. 29, 1115-1128.

Singh, A., Ulrich, K.-U., Giammar, D.E., 2010. Impact of phosphate on U (VI) immobilization in the presence of goethite. Geochimica et Cosmochimica Acta. 74, 6324-6343.

Sivaswamy, V., Boyanov, M.I., Peyton, B.M., Viamajala, S., Gerlach, R., Apel, W.A., Sani, R.K., Dohnalkova, A., Kemner, K.M., Borch, T., 2011. Multiple mechanisms of uranium immobilization by *Cellulomonas sp.* strain ES6. Biotechnology and Bioengineering. 108, 264-276.

Stemig, A.M., Do, T.A., Yuwono, V.M., Arnold, W.A., Penn, R.L., 2014. Goethite nanoparticle aggregation: effects of buffers, metal ions, and 4-chloronitrobenzene reduction. Environmental Science: Nano. 1, 478-487.

Stoliker, D.L., Campbell, K.M., Fox, P.M., Singer, D.M., Kaviani, N., Carey, M., Peck, N.E., Bargar, J.R., Kent, D.B., Davis, J.A., 2013. Evaluating Chemical Extraction Techniques for the Determination of Uranium Oxidation State in Reduced Aquifer Sediments. Environmental Science & Technology. 47, 9225-9232.

Stylo, M., Alessi, D.S., Shao, P.P., Lezama-Pacheco, J.S., Bargar, J.R., Bernier-Latmani, R., 2013. Biogeochemical Controls on the Product of Microbial U(VI) Reduction. Environmental Science & Technology. 47, 12351-12358.

Sunder, S., Shoesmith, D.W., Lemire, R.J., Bailey, M.G., Wallace, G.J., 1991. The effect of pH on the corrosion of nuclear fuel (UO_2) in oxygenated solutions. Corrosion Science. 32, 373-386.

Ulrich, K.-U., Ilton, E.S., Veeramani, H., Sharp, J.O., Bernier-Latmani, R., Schofield, E.J., Bargar, J.R., Giammar, D.E., 2009. Comparative dissolution kinetics of biogenic and chemogenic uraninite under oxidizing conditions in the presence of carbonate. Geochimica et Cosmochimica Acta. 73, 6065-6083.

Ulrich, K.U., Singh, A., Schofield, E.J., Bargar, J.R., Veeramani, H., Sharp, J.O., Bernier-Latmani, R., Giammar, D.E., 2008. Dissolution of biogenic and synthetic UO_2 under varied reducing conditions. Environmental Science & Technology. 42, 5600-5606.

Vecchia, E.D., Veeramani, H., Suvorova, E.I., Wigginton, N.S., Bargar, J.R., Bernier-Latmani, R., 2010. U(VI) reduction by spores of *Clostridium acetobutylicum*. Research in Microbiology. 161, 765-771.

Veeramani, H., Alessi, D.S., Suvorova, E.I., Lezama-Pacheco, J.S., Stubbs, J.E., Sharp, J.O., Dippon, U., Kappler, A., Bargar, J.R., Bernier-Latmani, R., 2011. Products of abiotic U(VI) reduction by biogenic magnetite and vivianite. Geochimica et Cosmochimica Acta. 75, 2512-2528.

Wang, X., Johnson, T.M., Lundstrom, C.C., 2015. Low temperature equilibrium isotope fractionation and isotope exchange kinetics between U(IV) and U(VI). Geochimica et Cosmochimica Acta. 158, 262-275.

Wang, Y., Bagnoud, A., Suvorova, E., McGivney, E., Chesaux, L., Phrommavanh, V., Descostes, M., Bernier-Latmani, R., 2014. Geochemical Control on Uranium(IV) Mobility in a Mining-Impacted Wetland. Environmental Science & Technology. 48, 10062-10070.

Watson, D.B., Wu, W.-M., Mehlhorn, T., Tang, G., Earles, J., Lowe, K., Gihring, T.M., Zhang, G., Phillips, J., Boyanov, M.I., Spalding, B.P., Schadt, C., Kemner, K.M., Criddle, C.S., Jardine, P.M.,

Brooks, S.C., 2013. In Situ Bioremediation of Uranium with Emulsified Vegetable Oil as the Electron Donor. Environmental Science and Technology. 47, 6440-6448.

Wellman, D.M., Icenhower, J.P., Gamerdinger, A.P., Forrester, S.W., 2006. Effects of pH, temperature, and aqueous organic material on the dissolution kinetics of meta-autunite minerals, (Na, $Ca)_{2-1}[(UO_2)(PO_4)]_2 \cdot 3H_2O$. American Mineralogist. 91, 143-158.

Williams, K.H., Bargar, J.R., Lloyd, J.R., Lovley, D.R., 2013. Bioremediation of uranium-contaminated groundwater: a systems approach to subsurface biogeochemistry. Current Opinion in Biotechnology. 24, 489-497.

Yabusaki, S.B., Fang, Y., Long, P.E., Resch, C.T., Peacock, A.D., Komlos, J., Jaffe, P.R., Morrison, S.J., Dayvault, R.D., White, D.C., 2007a. Uranium removal from groundwater via *in situ* biostimulation: Field-scale modeling of transport and biological processes. Journal of contaminant hydrology. 93, 216-235.

Yabusaki, S.B., Fang, Y., Long, P.E., Resch, C.T., Peacock, A.D., Komlos, J., Jaffe, P.R., Morrison, S.J., Dayvault, R.D., White, D.C., Anderson, R.T., 2007b. Uranium removal from groundwater via in situ biostimulation: Field-scale modeling of transport and biological processes. Journal of Contaminant Hydrology. 93, 216-235.

Zachara, J.M., Long, P.E., Bargar, J., Davis, J.A., Fox, P., Fredrickson, J.K., Freshley, M.D., Konopka, A.E., Liu, C., McKinley, J.P., Rockhold, M.L., Williams, K.H., Yabusaki, S.B., 2013. Persistence of uranium groundwater plumes: Contrasting mechanisms at two DOE sites in the groundwater–river interaction zone. Journal of Contaminant Hydrology. 147, 45-72.

Figures and Tables

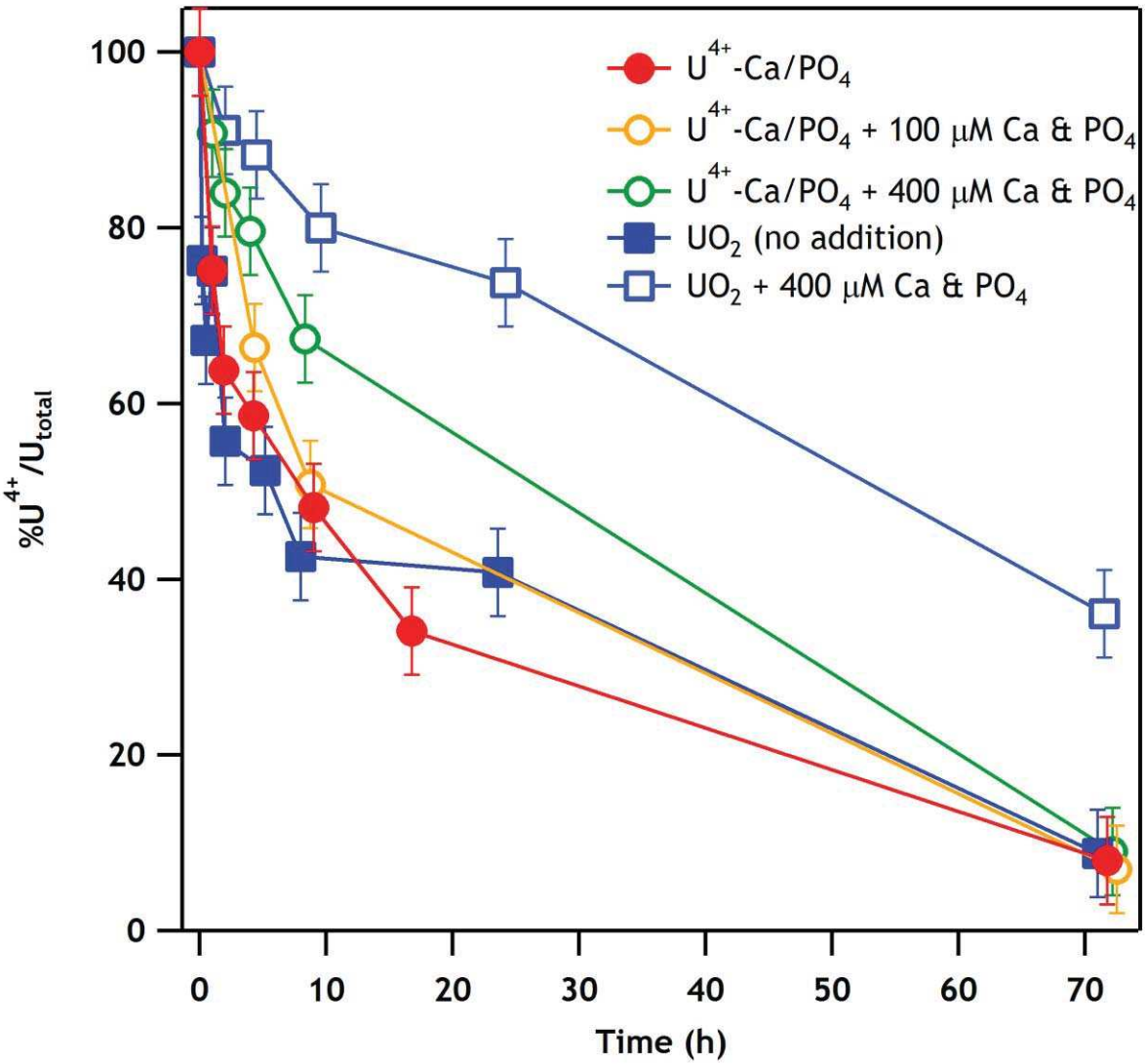

Fig. 1. Oxidation of UO_2 (squares) and U^{IV}-phosphate (circles) with (open markers) and without (closed markers) amendments of 100 and 400 µM $Ca^{2+}$and phosphate in neutral (pH 7.0) 5 mM MOPS buffer and 15 mM $NaClO_4$ supporting electrolyte. U^{IV} percentages are determined from linear combination fitting of XANES spectra using the starting U^{IV} material and U^{VI} precipitated in the presence or absence of Ca^{2+} and phosphate. In the case of UO_2 alone, a U^{VI} precipitate without added Ca^{2+} or PO_4^{3-} was used as the endmember.

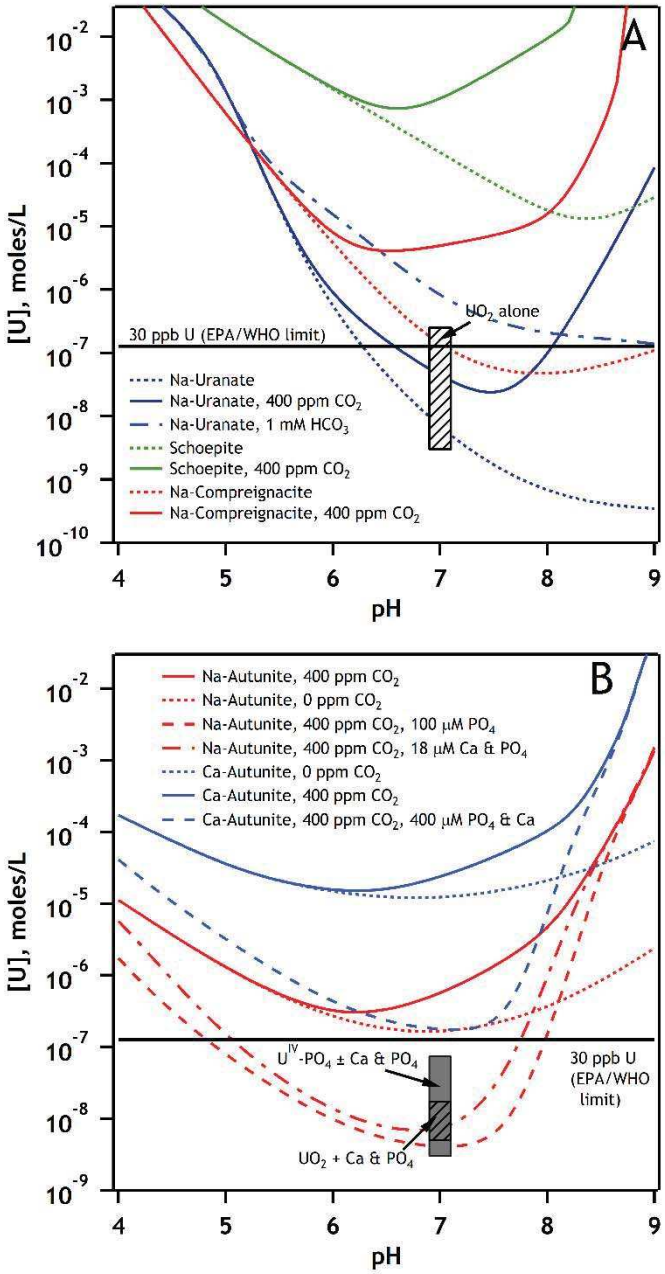

Fig. 2. Semi-log plot of uranium solubility in (A) Na containing solutions with schoepite and sodium-uranate endmembers. The Na-uranate endmember is calculated for solubility product of $K_{sp} = 10^{8.81}$ (Giammar and Hering, 2004). Na-compreignacite solubility is calculated using the solubility constant in Gorman-Lewis et al (2008). (B) Na-Ca-PO_4 solutions relevant to the oxidation of U^{IV}-phosphate species used in this study as well as UO_2 oxidation in solutions containing added Ca and phosphate. Sodium and calcium bearing autunite solubility is calculated for systems with and without atmospheric CO_2, and with and without fixed aqueous phase Ca and PO_4 concentrations. The grey bar indicates the range of measured U concentrations in the U^{IV}-phosphate oxidation experiments, and the hatched bar represents an upper estimate of U solubility in the UO_2 oxidation experiment with added Ca and PO_4.

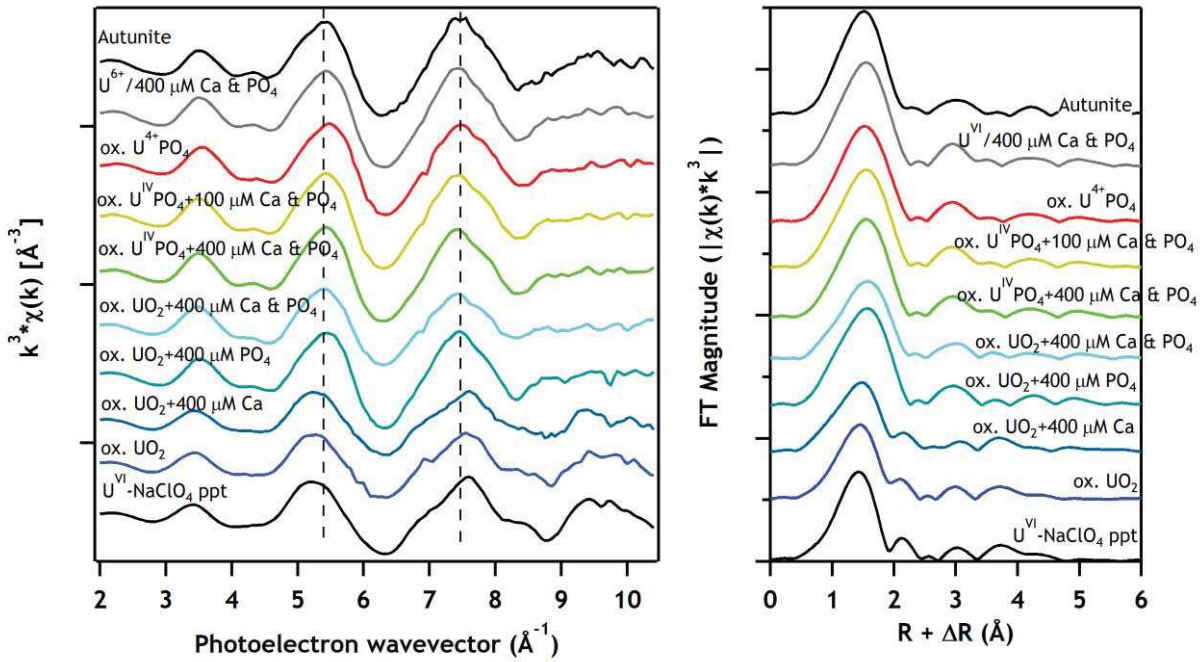

Fig. 3. Uranium L_{III} extended x-ray absorption fine structure spectra and the Fourier transformed spectra of U^{IV} products reacted with O_2 in the absence and presence of 100 and 400 μM Ca and/or PO_4 for 72 hours (determined to be predominantly U^{VI}). The experimental spectra are compared to a U^{VI}-oxyhydroxide precipitated from the MOPS/$NaClO_4$ buffer used in this study, autunite ($Ca(UO_2)_2(PO_4)_2 \cdot 12H_2O$), and 100 μM U^{VI} precipitated from a solution of 400 μM Ca and PO_4 in 5 mM MOPS buffer with a pH of 7.0 and 15 mM $NaClO_4$ background electrolyte. The dashed lines are an aid to the eye.

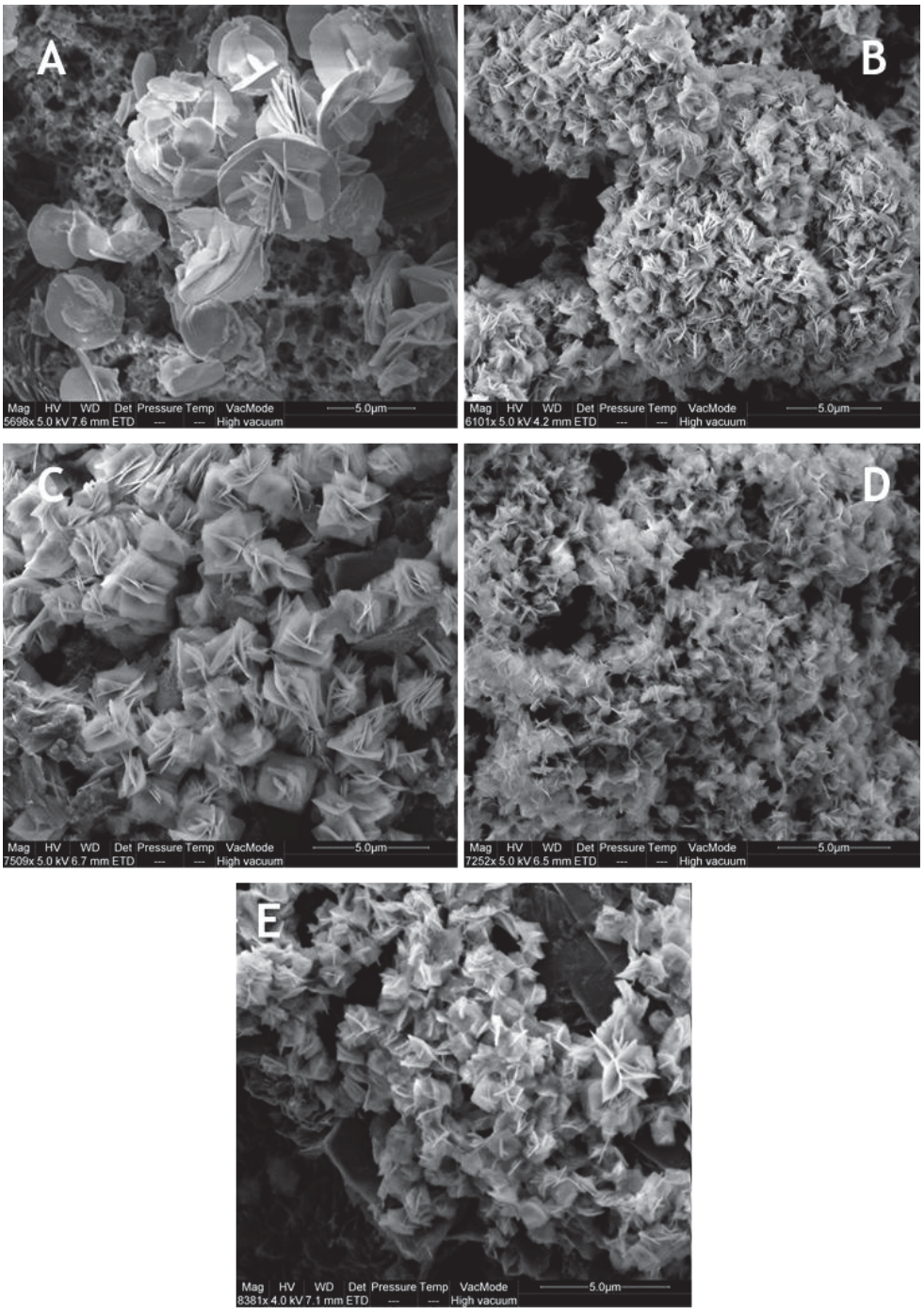

Fig. 4. SEM images of the products formed after oxidation of U^{IV} solids for 72 hours. (A) oxidized UO_2 with no additions of Ca or PO_4. (B) Oxidized UO_2 with 400 µM added Ca and PO_4. (C) Oxidized U^{VI}-PO_4 with no additions. (D) Oxidized U^{IV}-PO_4 with 100 µM added Ca and PO_4. (E) U^{IV}-PO_4 with 400 µM added Ca and PO_4. Scale bars are 5 µm.

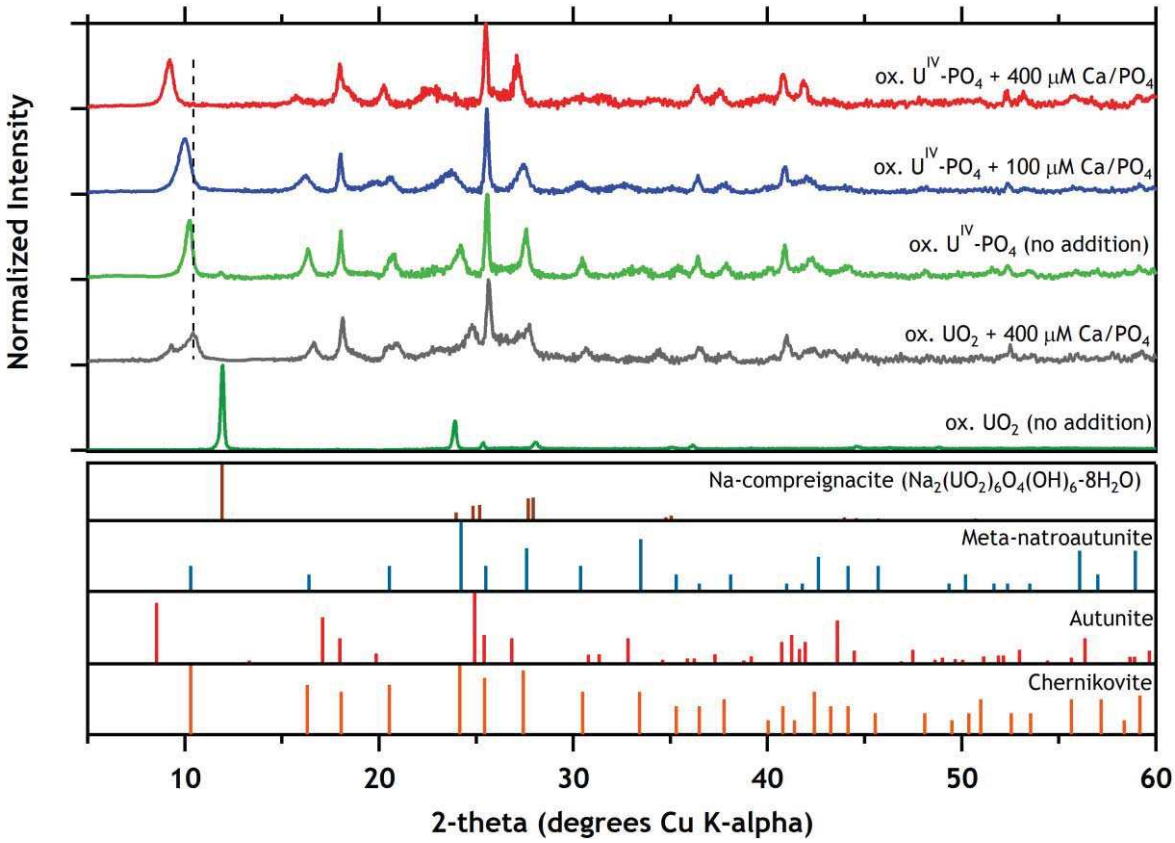

Fig. 5. X-ray diffraction (Cu K-alpha radiation) showing the effect of solution composition and U^{IV} starting material on U oxidation products formed after 72 hours in 5 mM MOPS and 15 mM $NaClO_4$ buffer solution with a pH of 7.0. The bars at the bottom of the plot show reference powder patterns for Na-compreignacite ($Na_2(UO_2)_6O_4(OH)_6{\cdot}8H_2O$), metanatroautunite ($Na_2(UO_2)_2(PO_4)_2{\cdot}8H_2O$), autunite ($Ca(UO_2)_2(PO_4)_2{\cdot}10H_2O$), and chernikovite ($(H_3O)_2(UO_2)_2(PO_4)_2{\cdot}6H_2O$). The dashed line is a guide for the eye, showing the shift in the patterns of solids with and without added Ca.

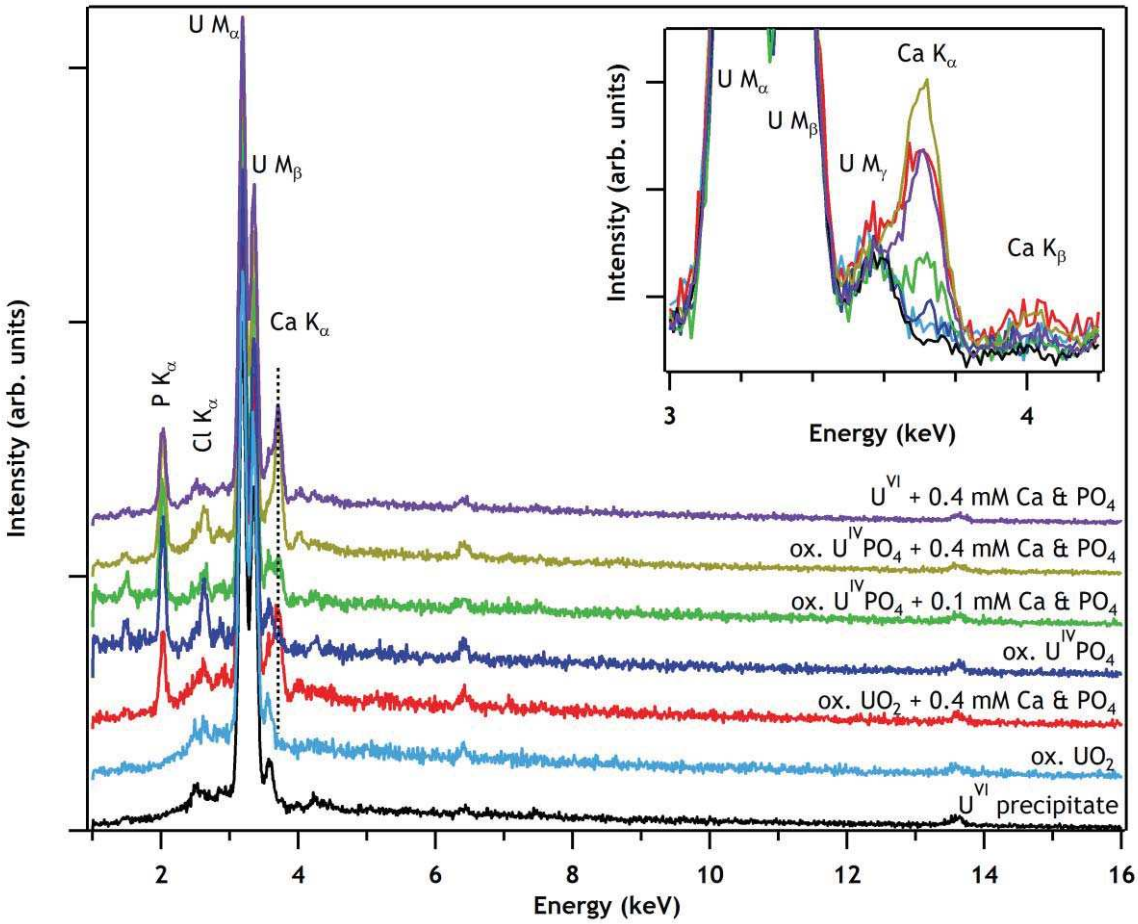

Fig. 6. Energy dispersive x-ray (EDX) spectra of U^{IV} products oxidized for 72 hours in 5 mM MOPS/15 mM $NaClO_4$ solution buffered at pH 7.0. Spectra are normalized to the U M_α line. The top and bottom spectra are 100 µM U^{VI} precipitated from 400 µM Ca and PO_4 solution and 100 µM U^{VI} precipitated in the absence of Ca and PO_4 both in 5 mM MOPS/15 mM $NaClO_4$ solution buffered to pH 7.0, respectively. Inset: expanded view of U M and Ca K_α x-ray fluorescence lines.

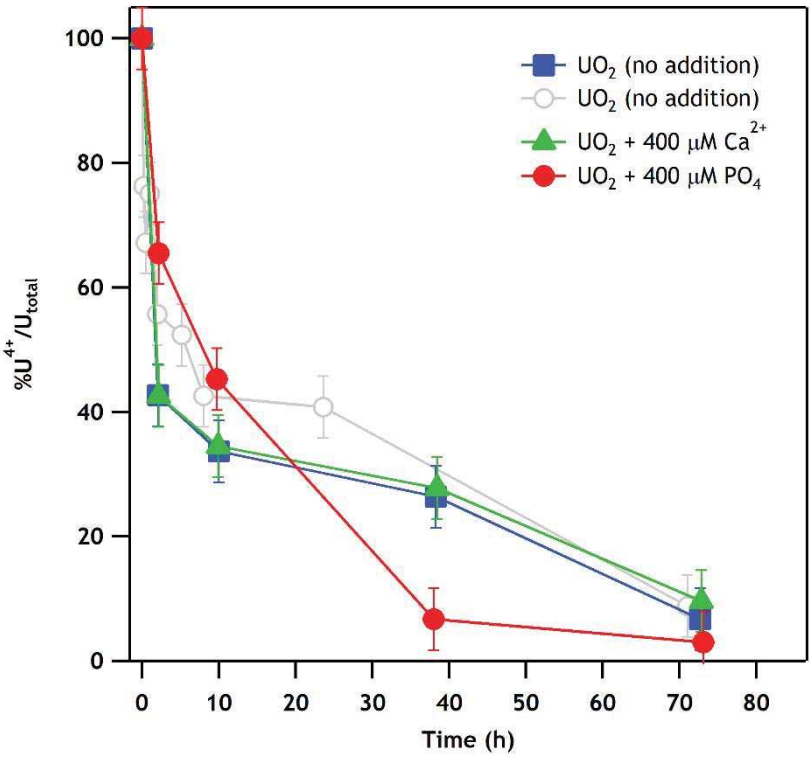

Fig. 7. Oxidation of UO_2 alone (Batch 2: blue squares) and with addition of 400 µM calcium (green triangles) or phosphate addition (red circles) in neutral (pH 7.0) 5 mM MOPS buffer and 15 mM $NaClO_4$ supporting electrolyte. Data from this experiment with the Batch 2 UO_2 solids show excellent agreement with those from Fig. 1 for the Batch 1 UO_2 solids (grey circles). U^{IV} percentages are determined from linear combination fitting of XANES spectra using the starting UO_2 material and U^{VI} precipitated in the presence or absence of Ca^{2+} and phosphate. In the case of UO_2 alone, a U^{VI} precipitate without added Ca^{2+} or PO_4^{3-} was used as the endmember. U^{IV}/U_{total} was determined using XANES LC fitting.

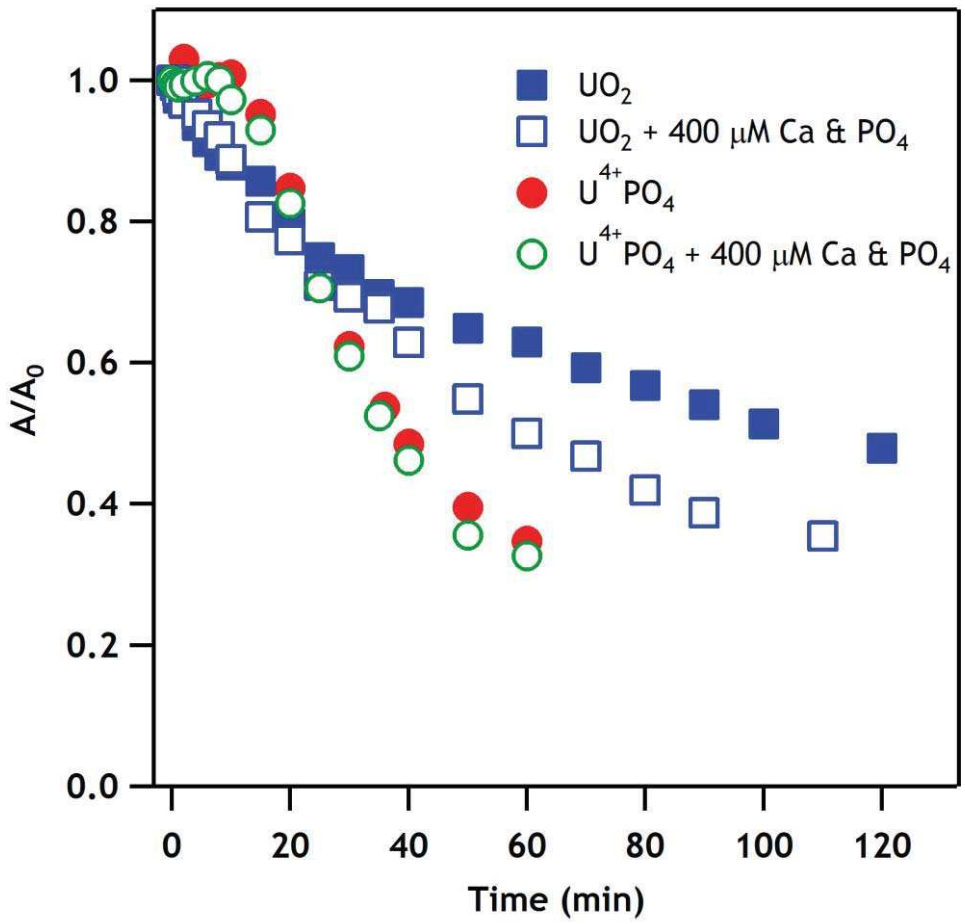

Fig. 8. Sedimentation of U^{IV}-phosphate and UO_2 suspensions at pH 7.0. Particles were suspended in 5 mM MOPS/15 mM $NaClO_4$ solution with and without 400 μM added Ca and PO_4. Normalized absorbance values (A/A_0) correspond to the amount of light (λ = 500 nm) absorbed by a 100 μM U_{solid} suspensions in 1-cm path-length cells.

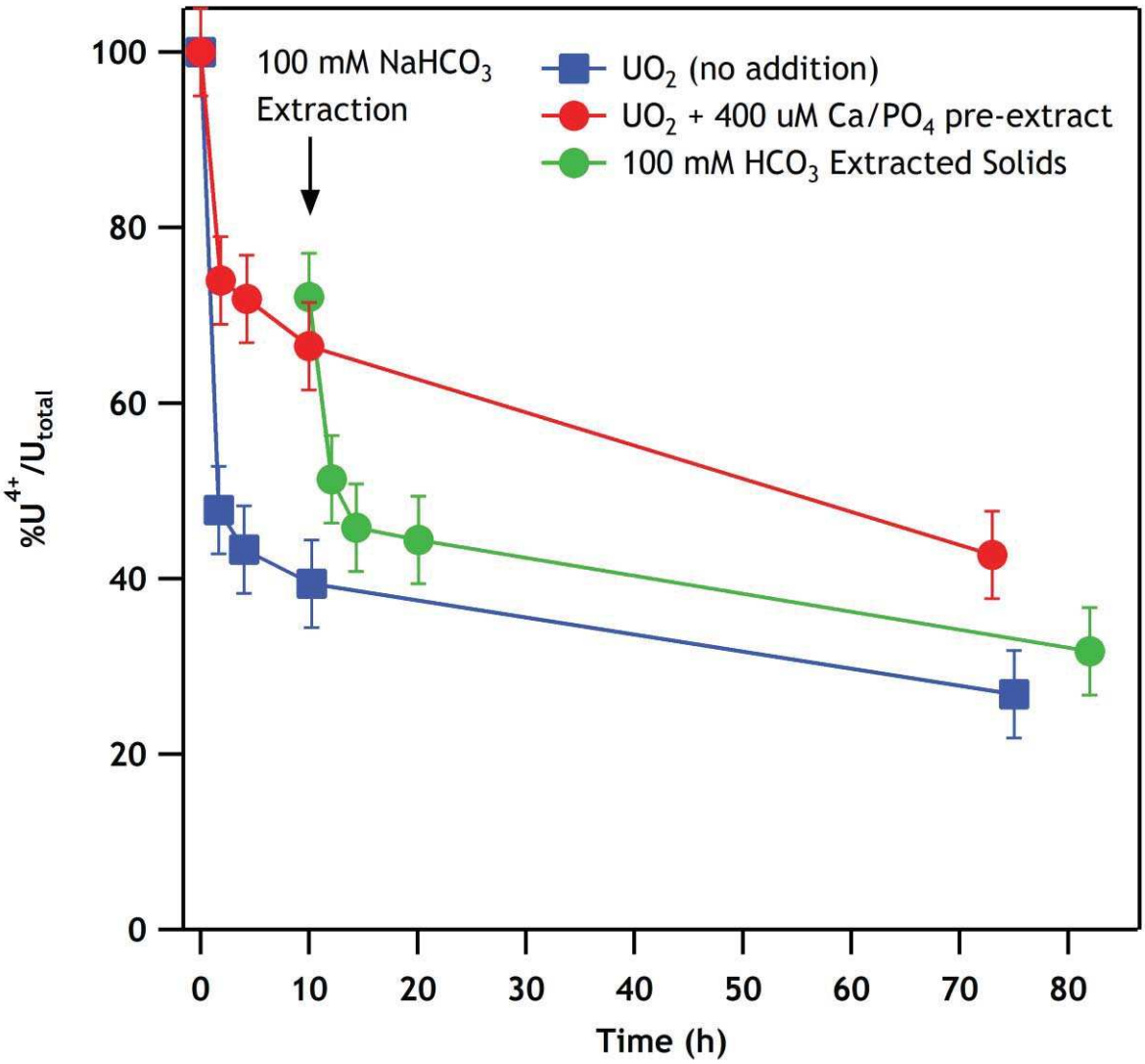

1074

1075 Fig. 9. Comparison of UO_2 oxidation in the presence (red) and absence (blue) of 400 µM added Ca/PO_4 to
1076 that of solids oxidized in the presence of 400 µM Ca and PO_4 then extracted with 100 mM $NaHCO_3$
1077 (pH 8.2) (green). Extracted solids were subsequently re-added to oxygen containing buffer not containing
1078 Ca and PO_4.

1079

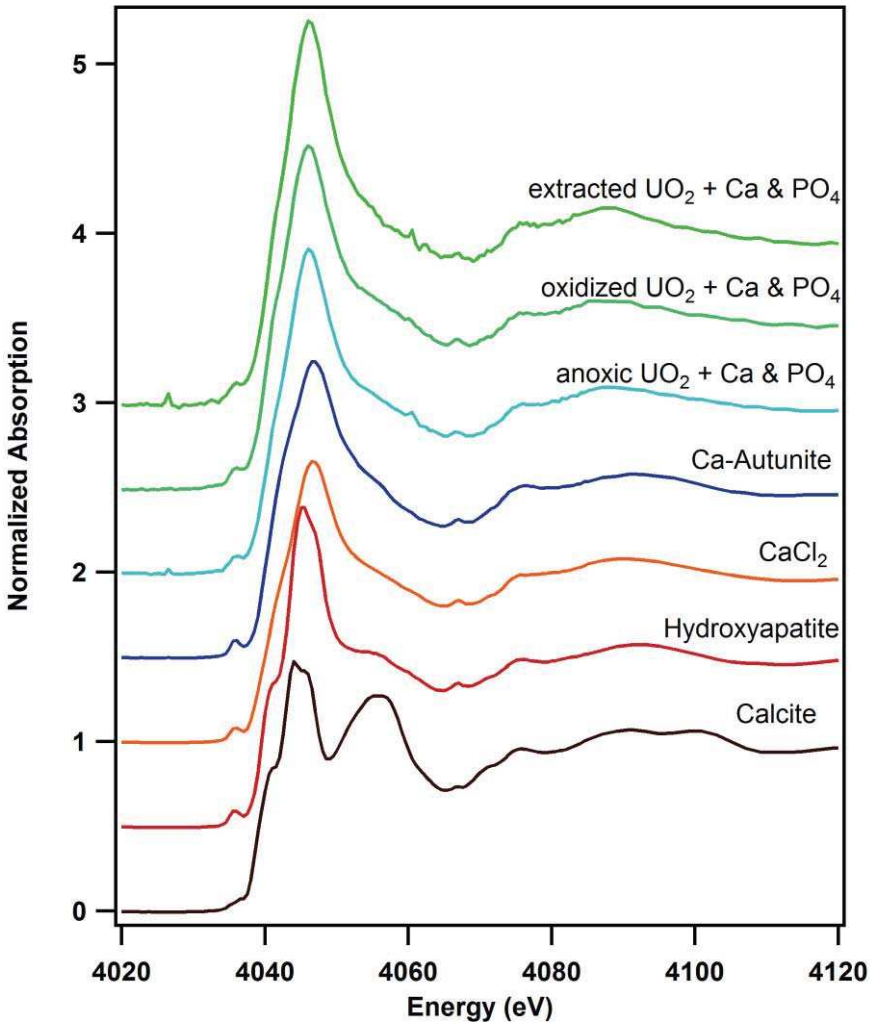

Fig. 10. Calcium K-edge XANES of UO_2 samples exposed to calcium and phosphate under anoxic conditions, after 10 hours of oxidation, and after extraction of the oxidized material with 100 mM bicarbonate. Samples are compared to standards of: calcium carbonate (calcite), calcium phosphate (hydroxyapatite), calcium autunite, and calcium chloride (1 M solution).

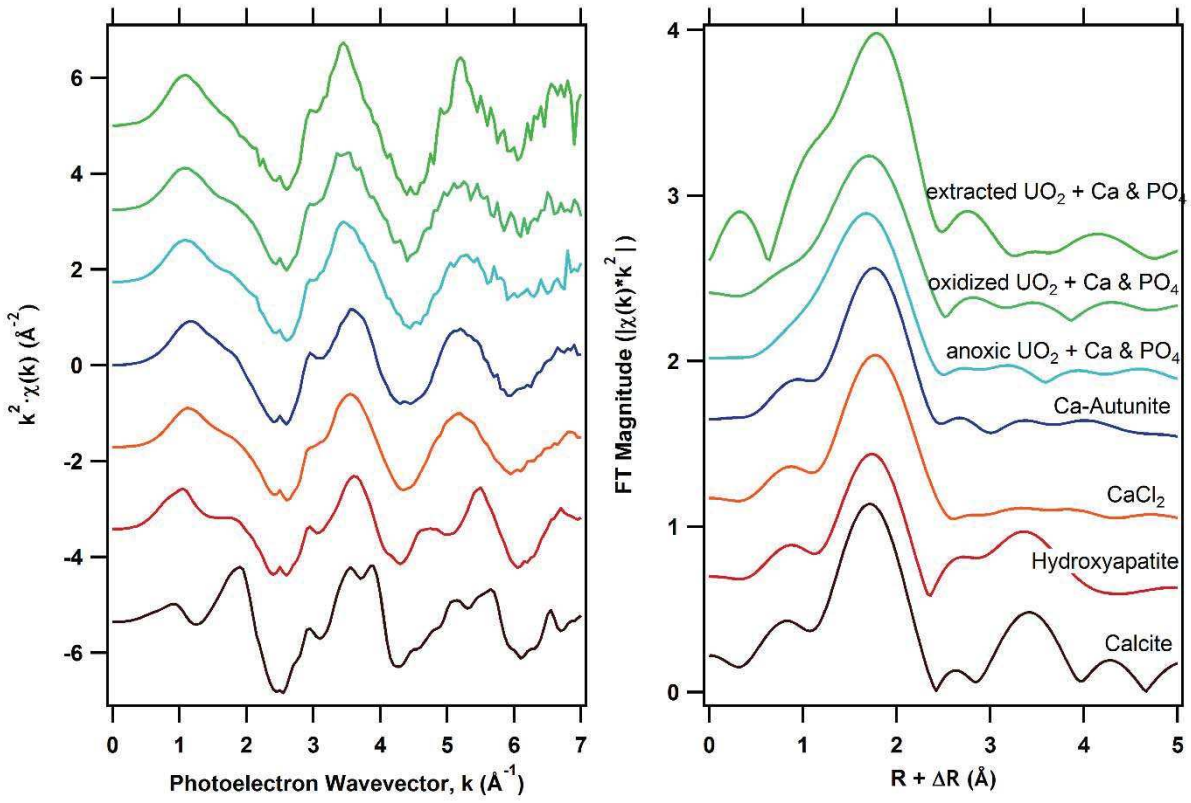

1085

1086 Fig. 11. Calcium K-edge EXAFS of UO_2 samples exposed to calcium and phosphate under anoxic
1087 conditions, after 10 hours of oxidation, and after extraction of the oxidized material with 100 mM
1088 bicarbonate. Samples are compared to standards of calcium carbonate (calcite), calcium phosphate
1089 (hydroxyapatite), calcium autunite, and calcium chloride (1 M solution).

1090

1091 Table 1 Rate constants for U^{IV} solids oxidation under various solution conditions.

Solid	Solution Conditions	Observed Oxidation Rate Constant, k_{obs}	Average Surface Area Normalized Rate Constant, k_{SA}
Nano-uraninite (batch 1)	Buffer[a]	0.23 ± 0.084 h^{-1} [b]	1.4×10^{-8} m/s[e]
Nano-uraninite (batch 2)	Buffer[a]	0.087 ± 0.065 h^{-1} [b]	SA not determined
Nano-uraninite (batch 3)	Buffer[a]	0.20 ± 0.11 h^{-1} [b]	SA not determined
Average nano-uraninite	Buffer[a]	0.17 ± 0.075 h^{-1} [c]	
Nano-uraninite (batch 1)	400 µM Ca and PO_4[a]	0.022 ± 0.0036 h^{-1} [b]	0.14×10^{-8} m/s
Nano-uraninite (batch 3)	400 µM Ca and PO_4[a]	0.074 ± 0.043 h^{-1} [b]	SA not determined
Nano-uraninite (batch 2)	400 µM Ca[a]	0.084 ± 0.066 h^{-1} [b]	SA not determined
Nano-uraninite (batch 2)	400 µM PO_4[a]	0.068 ± 0.0046 h^{-1} [b]	SA not determined
U^{IV}-phosphate (batch 1)	Buffer[a]	0.12 ± 0.099 h^{-1} [b]	0.9×10^{-8} m/s
U^{IV}-phosphate (batch 2)	Buffer[a]	0.476 h^{-1} [d]	2.7×10^{-8} m/s
Average U^{IV}-phosphate	Buffer[a]	0.30 h^{-1}	
U^{IV}-phosphate (batch 1)	100 µM Ca and PO_4[a]	0.077 ± 0.0098 h^{-1} [b]	0.57×10^{-8} m/s
U^{IV}-phosphate (batch 1)	400 µM Ca and PO_4[a]	0.044 ± 0.0056 h^{-1} [b]	0.33×10^{-8} m/s
U^{IV}-phosphate (batch 2)	1 mM Ca and PO_4[a]	0.055 ± 0.019 h^{-1} [b]	0.32×10^{-8} m/s
U^{IV}-phosphate (batch 2)	1 mM Ca and PO_4 + 10 mM $NaHCO_3$	0.039 ± 0.012 h^{-1} [b]	0.22×10^{-8} m/s

1092 [a] 5 mM MOPS buffer prepared with a pH of 7.0 and with 15 mM $NaClO_4$ background electrolyte.

1093 [b] Error term in fitting $ln(U^{IV}/U_{total})$ vs. time (1 σ).

1094 [c] Error term, standard deviation of triplicate experiments.

1095 [d] Estimated from the slope at t = 0 and 2 hours.

1096 [e] m/s = 1000 liters m^{-2} s^{-1}.

Table 2. XANES and EXAFS fitting results and aqueous concentrations of U, Ca, and PO_4 for oxidation of UO_2 and U^{IV}-phosphate in 5 mM MOPS/15 mM $NaClO_4$ buffer with and without 400 µM added Ca and PO_4, as shown in Fig. 1.

	Solids—XANES LC Fits			Solids—EXAFS LC Fits			Aqueous Phase		
Reaction Time (h)	**%U^{IV}**	**%U^{VI}**	**χ_v^2**	**% U^{IV}**	**% U^{VI}**	**χ_v^2**	**[U], µM**	**[Ca^{2+}], µM**	**[PO_4^{3-}], µM**
UO_2 with no added Ca^{2+} or PO_4^{3-}									
0	100	0	-	100	0	-	b.d.l.[a]	b.d.l.[c]	n.m.[d]
0.2	76.3	23.7	4.00×10^{-4}	72	28	0.291	0.050[b]	b.d.l.	n.m.
0.5	67.2	32.8	6.25×10^{-4}	73	27	0.301	b.d.l.[a]	b.d.l.	n.m.
1.0	75.1	24.9	3.66×10^{-4}	79	21	0.293	b.d.l.[a]	b.d.l.	n.m.
2.0	55.7	44.3	3.91×10^{-4}	66	34	0.324	0.25[b]	b.d.l.	n.m.
5.2	52.4	47.6	3.95×10^{-4}	63	37	0.325	b.d.l.[a]	b.d.l.	n.m.
8.0	42.6	57.4	5.19×10^{-4}	56	44	0.414	0.19[b]	b.d.l.	n.m.
23.6	40.8	59.2	4.71×10^{-4}	51	49	0.372	0.032[b]	b.d.l.	n.m.
71.0	8.8	91.2	1.12×10^{-4}	12	88	0.148	0.003[b]	b.d.l.	n.m.
UO_2 + 400 µM Ca^{2+} and PO_4^{3-}									
0	100	0	-	100	0	-	b.d.l.[a]	377	429
2.0	91.1	8.9	0.13×10^{-4}	91	9	0.138	b.d.l.[a]	349	340
4.5	88.3	11.7	0.19×10^{-4}	89	11	0.140	b.d.l.[a]	342	331
9.6	80	20	0.63×10^{-4}	85	15	0.216	b.d.l.[a]	349	356
24.2	73.8	26.2	1.71×10^{-4}	75	25	0.212	b.d.l.[a]	412	335
71.5	36.1	63.9	0.53×10^{-4}	33	67	0.095	b.d.l.[a]	327	301
U^{IV}-phosphate with no added Ca^{2+} or PO_4^{3-}									
0	100	0	-	100	0	-	0.005[b]	16.1	10.5
1	75.2	24.8	0.13×10^{-4}	84	16	0.079	0.073[b]	19.0	11.1
1.9	63.8	36.2	0.46×10^{-4}	74	26	0.102	0.012[b]	18.6	14.5
4.3	58.6	41.4	0.21×10^{-4}	74	26	0.070	0.008[b]	18.6	16.3
9.0	48.2	51.8	0.56×10^{-4}	64	36	0.113	0.050[b]	17.4	17.7
16.8	34.1	65.9	0.69×10^{-4}	48	52	0.133	0.023[b]	25.0	9.2
71.8	8	92	0.51×10^{-4}	14	86	0.043	0.009[b]	23.0	2.1
U^{IV}-phosphate + 100 µM Ca^{2+} and PO_4^{3-}									
0	100	0	-	100	0	-	0.005[b]	97.1	97.5
4.33	66.4	33.6	0.07×10^{-4}	67	33	0.020	0.005[b]	95.6	91.5
8.8	50.8	49.2	0.04×10^{-4}	56	44	0.017	0.005[b]	95.3	88.0
72.5	7	93	0.01×10^{-4}	10	90	0.038	b.d.l.[a]	92.1	80.8
U^{IV}-phosphate + 400 µM Ca^{2+} and PO_4^{3-}									
0	100	0	-	100	0	-	0.005[b]	377	429
1.0	90.8	9.2	0.12	96	4	0.035	0.004[b]	344	363
2.0	84	16	0.21×10^{-4}	86	14	0.028	0.003[b]	352	349
4.0	79.6	20.4	0.02×10^{-4}	84	16	0.030	b.d.l.[a]	349	378
8.3	67.4	32.6	0.04×10^{-4}	75	25	0.042	b.d.l.[a]	344	356
72.2	9	91	0.11×10^{-4}	10	90	0.033	b.d.l.[a]	329	375

[a] b.d.l. = below detection limit, equal to [U] in HNO_3 blank (0.017 µM U) used to prepare samples for KPA analysis.

[b] [U] measured > detection limit of blank, the report concentration is the difference between the blank and the sample.

[c] b.d.l. = below detection limit, <0.25 µM Ca^{2+}.

[d] n.m. = not measured.

Table 3 XANES and EXAFS fitting results and aqueous concentrations of U, Ca, and PO_4 for oxidation of UO_2 in 5 mM MOPS/15 mM $NaClO_4$ buffer with and without 400 µM added Ca and PO_4 and after 100 mM bicarbonate extraction as shown in Fig. 8.

	Solids—XANES LC Fits			**Aqueous Phase**		
Reaction Time (h)	% U^{IV}	% U^{VI}	χ_v^2	[U], µM	[Ca^{2+}], µM	[PO_4^{3-}], µM
UO_2 without added Ca^{2+} and PO_4^{3-}						
0	100	0	-	n.m.[a]	n.m.[a]	n.m.[a]
1.7	47	52.5	8.18×10^{-4}	1.15	b.d.l.[b]	b.d.l.[b]
4	43	53	8.51×10^{-4}	1.68	b.d.l.[b]	b.d.l.[b]
10.3	39	61	9.26×10^{-4}	4.66	b.d.l.[b]	b.d.l.[b]
75	26	74	6.31×10^{-4}	1.52	b.d.l.[d]	b.d.l.[b]
UO_2 + 400 µM Ca^{2+} and PO_4^{3-} **pre-extraction**						
0	100	0	-	b.d.l.[b]	322	375
1.8	74	26	2.83×10^{-4}	b.d.l.[b]	322	381
4.3	72	28	2.83×10^{-4}	b.d.l.[b]	307	368
10	66	34	3.88×10^{-4}	b.d.l.[b]	317	371
73	43	57	4.15×10^{-4}			
100 mM anoxic bicarbonate extraction, pH 8.2						
14.5[c]	-	-	-	12.2	6.9	20
UO_2 + 400 µM Ca^{2+} and PO_4^{3-} **post-extraction**						
0[d]	72	28	5.18×10^{-4}	n.m.[a]	n.m.	n.m.
2.1	51	49	9.22×10^{-4}	b.d.l.[b]	3.37	b.d.l.[b]
4.3	46	54	8.69×10^{-4}	0.78	1.97	b.d.l.[b]
10.1	44	56	8.20×10^{-4}	0.64	10.1	b.d.l.[b]
72	31	69	7.31×10^{-4}	3.37	2.20	b.d.l.[b]

[a] n.m. = not measured.

[b] b.d.l. = below detection limit, approximately <0.25 µM Ca^{2+}, <0.4 µM U, <0.7 µM PO_4^{3-}.

[c] Solids were extracted for 14.5 hours.

[d] t = 0 is defined here as the starting point of oxidation after anoxic bicarbonate extraction and washing.